3-D Target Classification in Short Range Radar Applications

Arun Vijayaraghavan

Delft University of Technology

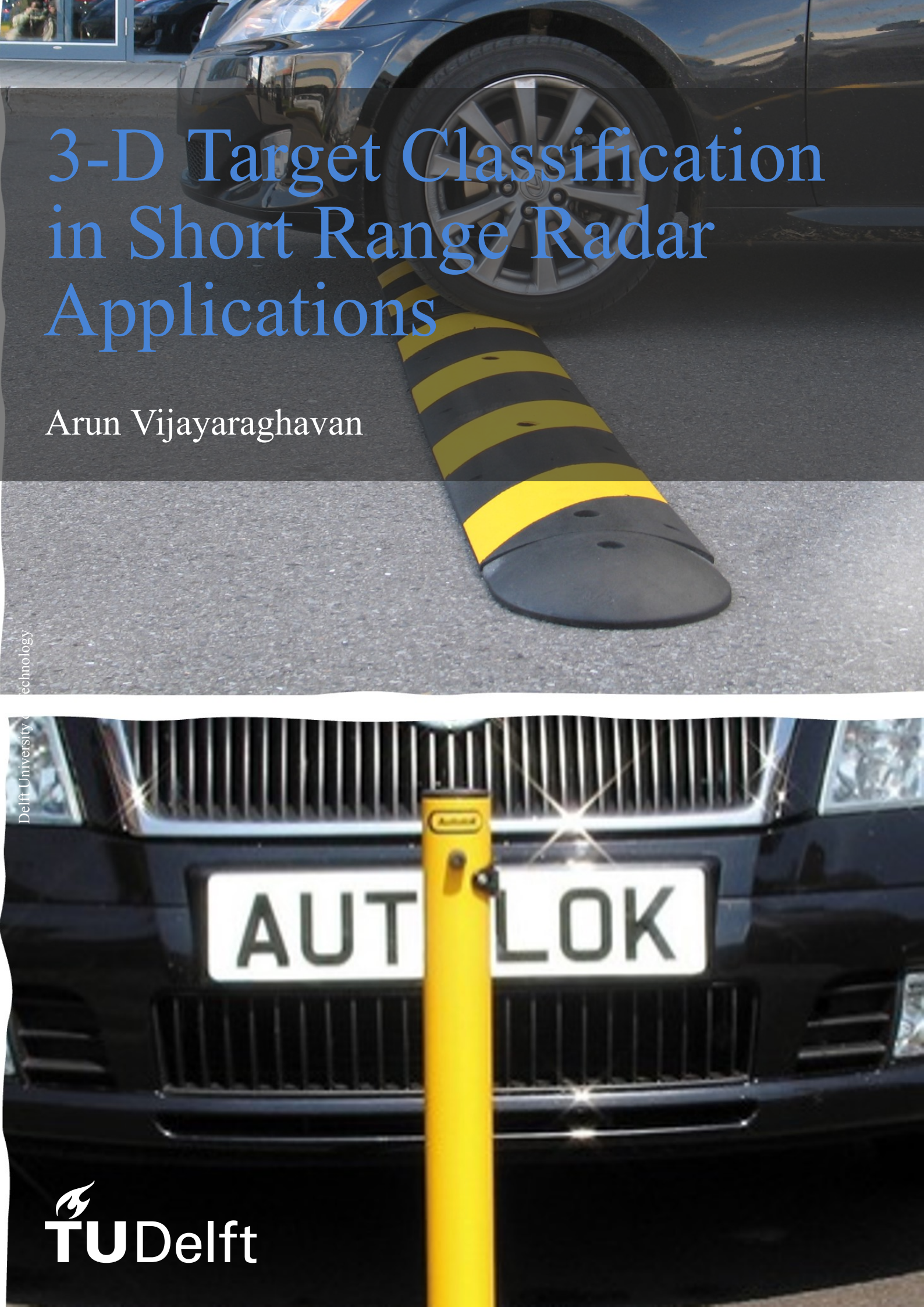

TU Delft

3-D Target Classification in Short Range Radar Applications

Master Thesis

by

Arun Vijayaraghavan

to obtain the degree of Master of Science
at the Delft University of Technology,
to be defended publicly on Thursday December 15, 2022 at 09:00 AM.

Student number:	4902351	
Thesis committee:	Prof. dr. A. Yarovoy,	TU Delft, supervisor
	Dr. F. Uysal,	TNO, Netherlands
	dr. ir. R. Heusdens,	TU Delft
	ir. Arie Koppelaar,	NXP Semiconductors

This thesis is confidential and cannot be made public until December 31, 2022.

TU Delft

Abstract

3-D Target Classification in Short range Radar Applications

Over the years in the automotive industry, the use of radar sensors in advanced driver assistant systems (ADAS) has been increasing, shining a light on various safety and security concerns to be dealt, that come along with it. The performances of existing sensor technologies such as camera, LIDAR and GPS can be very well complemented by the use of millimeter-wave radar due to its robust performance in various conditions.

In assisted or autonomous driving tasks, localization of targets and their height information is important to be determined. Since height information is lacking from automotive radar systems without elevation measurements capabilities, this remains a challenge to be worked on. In the application discussed in this thesis, using the radar specifications providing a high range and velocity resolution, the multi-paths can be resolved in the range-Doppler domain and be used for height estimation techniques. The automotive applications for which short and ultra-short range radar systems are used, require a high range and velocity resolution.

In this thesis, a low complexity and fast target height classification algorithm is presented using a FMCW radar. In the process of having a quick response automotive radar system, low latency DoA estimation technique was employed. To estimate the height properly, knowledge of the ego-velocity is needed. A histogram method can be used to roughly estimate the ego-velocity. The ego-velocity estimate can be refined using an Extended Kalman filter that tracks targets that are supposed to be annotated with height information. Using the vertical doppler beam sharpening technique, the improved ego-motion estimate helps in estimating the elevation angles of the targets and therefore, their corresponding height. An overview of the height estimation process is explained to provide a real time mapping of the target in 3-Dimensions, showcasing the improvement in ego-motion estimation leading to an elevation angle estimation. Simulations and experiments are carried out to validate and verify the algorithm. The results show promising results and also reveal potential improvements and the need for more simulations and experiments to mature the concept further.

$A.Vijayaraghavan$
Delft, December 2022

Acknowledgement

First and foremost, I would like to sincerely thank the Microwave Sensing, Signals and Systems (MS3) Group and NXP Semiconductors N.V. for giving me the opportunity to work on a Master Thesis project in my field of interest.

My supervisors prof.dr.Alexander Yarovoy (MS3) and Arie Koppelaar (NXP) need close attention as I cannot thank them more for the guidance and expertise they have provided during my thesis. Most importantly, the support extended during the toughest times and in prodiving the right motivation.. I highly respect the amount of valuable time they have put into me. Their office doors were always open, and they were willing to answer my questions at any moment. Also, I would like to thank Dr. Faruk Uysal for his support and guidance in the major portion of my thesis and his valuable in-depth and feedback. Furthermore, I would like to acknowledge Francesco Laghezza (NXP) for the engaging discussions on the height estimation techniques and its application in FMCW radar systems.

I would like to express my sincere gratitude to all my friends who ensured my well being and have been a constant source of support. Last but not the least, I cannot thank enough for the support of my family during the course of the project, in the challenging times and their belief in myself helped me in achieving the end goal of this thesis.

Contents

Preface i

Summary ii

Nomenclature v

1 Introduction 1
- 1.1 Motivation . . . 1
- 1.2 State of the art . . . 1
- 1.3 Novelty in the study . . . 2
- 1.4 Project Approach . . . 2
- 1.5 Outline of the thesis . . . 3

2 Fundamentals of Automotive Radar 4
- 2.1 Measurement Parameters . . . 4
- 2.2 Frequency Modulated Continuous Wave (FMCW) Radar . . . 4
- 2.3 Signal Model . . . 7
- 2.4 Super Resolution Techniques in DoA Estimation . . . 9
  - 2.4.1 MUltiple SIgnal Classification (MUSIC) . . . 10
  - 2.4.2 Estimation of Signal Parameters via Rotational Invariance Techniques (ESPRIT) . . . 10
- 2.5 Space-Time Adaptive Processing (STAP) . . . 10
- 2.6 Ego-motion . . . 10
  - 2.6.1 Ego-motion based on other modalities . . . 10
  - 2.6.2 SLAM-based ego-motion . . . 11
  - 2.6.3 Radar-based ego-motion . . . 11
- 2.7 Kalman Filter . . . 11
- 2.8 Height Estimation Techniques . . . 13
  - 2.8.1 Multipath Height Finding . . . 13
  - 2.8.2 Vertical Doppler Beam Sharpening . . . 15
  - 2.8.3 Conclusion . . . 16

3 Signal Processing Chain 17
- 3.1 Application Specifications . . . 17
- 3.2 DoA Estimation . . . 17
  - 3.2.1 MIMO-Monopulse . . . 18
  - 3.2.2 Amplitude Comparison Monopulse (ACM) . . . 19
  - 3.2.3 Phase Comparison Monopulse (PCM) . . . 22
- 3.3 Multipath distinction . . . 22
- 3.4 Geometry . . . 23
- 3.5 Flowchart of the proposed algorithm . . . 24
- 3.6 Ego-velocity estimation using velocity histogram . . . 25
- 3.7 Target tracking using Kalman Filter . . . 26
  - 3.7.1 Coordinate Conversion function . . . 27
  - 3.7.2 Conclusion . . . 29

4 Simulation Results 30
- 4.1 Simulation process . . . 31
- 4.2 Comparison . . . 34
- 4.3 Conclusion . . . 37

5 Experimental Validation 38
- 5.1 Measurement Setup . . . 38

5.2 Observations . . . 39
5.2.1 Conclusion . . . 43

6 Conclusion **44**
6.1 Results and Novelties . . . 44
6.1.1 Challenges met during this thesis project . . . 45
6.2 Future Recommendations . . . 45
6.2.1 3-Dimensional EKF . . . 45
6.2.2 Indirect path method . . . 46
6.2.3 Experimental test cases . . . 46

References **47**

A Validation Code Example **50**

B Coordinate Conversion function Derivations **51**

Nomenclature

Abbreviations

Abbreviation	Definition
ADAS	Advanced driver assistant systems
SRR	Short Range Radar
LRR	Long Range Radar
MRR	Medium Range Radar
FMCW	Frequency Modulated Continuous Wave
LFM	Linear Frequency Modulation
MIMO	Multiple-Input Multiple-Output
ULA	Uniform Linear Array
LSQ	Least Squares
RANSAC	Random Sample Consensus
LIDAR	Light Detection and Ranging
GPS	Global Positioning System
FFT	Fast Fourier Transform
EKF	Extended Kalman Filter
TDM	Time Division Multiplexing
CDM	Code Division Multiplexing
DDM	Doppler Division Multiplexing
FDM	Frequency Division Multiplexing
DoA	Direction of Arrival
DoD	Direction of Departure
SNR	Signal-to-Noise ratio
MUSIC	Multiple SIgnal Classification
ESPRIT	Estimation of Signal Parameters via Rotational Invariance Techniques
STAP	Space-Time Adaptive Processing
SLAM	Simultaneous Localization and Mapping
ACM	Amplitude Comparison Monopulse
PCM	Phase Comparison Monopulse
DBF	Digital Beamforming
LOS	Line-of-Sight
NLOS	Non Line-of-Sight

Symbols

Symbol	Definition	Unit
R	Range	[m]
ΔR	Range resolution	[m]
R_d	Radial distance	[m]
R_{max}	Maximum detectable range	[m]
v	Velocity	[m/s or km/h]
v_{max}	Maximum detectable velocity	[m/s or km/h]
Δv	Velocity resolution	[m/s]
v_r	Radial velocity	[m/s]
θ	Azimuth angle	[deg]

Symbol	Definition	Unit
$\Delta\theta$	Azimuth resolution	[deg]
φ	Elevation angle	[deg]
c	Speed of light	[m/s]
λ	Wavelength	[m]
T	Chirp duration	[s]
T_{Frame}	Frame or measurement duration	[s]
f_c	Carrier frequency	[Hz]
f_{beat}	Beat frequency	[Hz]
τ	Time delay	[s]
d	Virtual array inter-element spacing	[m]
d_{Tx}	Transmit array inter-element spacing	[m]
d_{Rx}	Receive array inter-element spacing	[m]
N	Number of antennas in virtual array	
M_{Tx}	Number of transmit antennas	
M_{Rx}	Number of receiver antennas	

1

Introduction

Automotive industry over the years have advanced when it comes to the involvement of radar sensors, which play a key role in the development of assisted and autonomous driving concepts and applications such as advanced driver assistant systems (ADAS). Their usage is expected to grow further in the coming years as well as corresponding safety and security concerns. Different sensor technologies have been active in providing the safety measures of the vehicle such as blind spot detection, collision avoidance and so on. The Millimeter-wave radar provides robust performances in low lighting and rough environmental conditions such as rain, compared to the other sensors in the market like camera, LIDAR and GPS (Global Positioning System) [1]. The radar technologies have developed from 24 GHz to 77-81GHz, thus allowing a better resolution. The modulation method employed in automotive radar is Frequency Modulated Continuous-Wave (FMCW) which holds advantages that include high resolution distance measurement, quick updating and low sampling frequency requirements of analog-to-digital converter. The radar transmits a burst of chirps and upon reflection from the target, a sequence of chirps is received. Based on these chirps, the range, velocity and angle are calculated. MIMO radar technology is used to determine the angle information of the targets. The applications of using automotive radar would include Adaptive Cruise control, brake assist, lane change, assist, target classification and so on. These respective automotive applications fall under three radar classifications, namely Short Range Radar (SRR), Medium Range Radar (MRR) and Long Range Radar (LRR). Adaptive Cruise control falls under the LRR, lane change assist under MRR and obstacle detection under SRR, with it requiring a better range resolution comparatively [2].

1.1. Motivation

In today's world, with increase in the growth of automotive industry, as mentioned before, the spotlight has been shining bright on the safety of drivers, passengers and pedestrians and the reliability provided by the automotive radar system. There are multiple targets present on the road and to guarantee safety, detecting these targets in a reliable fashion or localization is important. While performing assisted or autonomous driving tasks, one of the challenges is to determine, using automotive radar system, whether it is possible to drive under, over or through certain objects in the driving direction or within the maneuvering area of the car. However, this is not a simple task for automotive radar systems since an object detection in the driving direction does not contain height information. The automotive applications for which short and ultra-short range radar systems are used, require a high range and velocity resolution. In such case, the multi-path components can be separated from the the direct path, thus enabling height estimation techniques in the range and Doppler domain which can be used to retrieve the height information of the target. Having an extra information on the elevation angle of the target can further improve the height classification of the targets for instance, in the case of overhead structures.

1.2. State of the art

As mentioned in the motivation, the classifications of the target can be improved using azimuth and elevation angle estimation. Hence, selecting a DoA estimation technique adhering to the application requirements, such as low latency, is a significant issue. In general radar applications, the performances of super-resolution algorithms such as MUSIC and ESPRIT in DoA estimations, which are considered to be state-of-the-art, are well documented

[3][4]. However, the estimation performance suffers when few measurements are available and the computational cost is high, which is not desired in quick response automotive radar system. The concept of Monopulse is a well established technique in DoA estimation due to its benefits in computational cost and ability to work with few measurements as compared to MUSIC and ESPRIT [5].

Furthermore, the velocity of the automobile also plays a significant role in the height estimation of the targets as we are dealing with relative velocities. The dependency of the relative velocity estimates in height estimation techniques such as vertical doppler beam sharpening makes ego-motion estimation a crucial aspect of the algorithm. In vertical doppler beam sharpening, the height of the object is determined from the doppler frequency shift induced by the target's velocity relative to the radar [6]. Thus far, many publications are also present on providing various ego-motion estimation techniques such as analysis on the measured radial velocity over the azimuth position of targets being done along with RANSAC (fitting algorithm) [7]. LSQ (Least Squares) estimators are also used to reduce significant bias error. D. Kellner et al. through the publications has explained the ego-motion estimation using single and multiple doppler radars [8][9]. However, elevation angle is not being used in any part of the analysis. Also, T. Miyasaka et al. published a study on laser-based ego-motion estimation using multi-layer LIDAR mounted on the bumper of the vehicle [10]. The ego-motion obtained by the standard vehicle odometry i.e. through wheel-based odometry and inertial sensing (gyroscopes and accelerometers), is a good estimation of the velocity of the automobile. But it comes with an uncertainty that increases with increase in the dynamic movement of the vehicle e.g. drift [11][12]. The unevenness of the terrain also aids to the error along with systematic errors caused by kinematic imperfections e.g. unequal wheelbase.

An error in ego-velocity estimation and absence of angle information can alter the localization of targets and produce a non-reliable result, thereby, putting the driver and other road users in danger. Literature has been provided on estimating ego-velocity based on azimuth angle and various target localization algorithms in collaboration with SLAM. Furthermore, Robin van Gaalen did a study on localization of autonomous vehicle based on radar and LIDAR Fusion, also in collaboration with NXP Semiconductors for this M.Sc. Thesis at Delft University of Technology [13]. However, the velocity estimator employed was biased as elevation angles were not incorporated. Multiple ideas to refine the DoA estimation, so as to improve the height and ego-motion estimation accuracy were suggested to be applied, i.e. using MUSIC algorithm or different target detection schemes, and using SLAM algorithms.

1.3. Novelty in the study

The research objective of the thesis is to achieve a fast and low-complexity algorithm providing a reliable estimate of ego-velocity and target classification inclusive of elevation angle.

This thesis aims to contribute novelty in the following aspects:

1. Investigating how a classical tracker needs to be modified to address a different clustering approach which includes ego-velocity.
2. Inspecting the improvement in height estimation and localization procedure by adding the dependency of elevation angle to the current ego-velocity estimation which are based only on azimuth behaviour.

1.4. Project Approach

This thesis will provide a study on how the use of elevation angle and multipath improves the classification as well as ego-motion estimation in a fast, low-complex manner using a certain array configuration. The property of multipaths can be used in the association of targets. The monopulse technique provides a fast and precise estimate of the azimuth positions of the targets using limited available measurements. An analysis on the measured radial velocities of the target is done, which contains the information of the azimuth position of the targets as well as the elevation angles. The distribution of this velocity profile inclusive of elevation angle information is analyzed and improved over the course using an Extended Kalman Filter (EKF). The use of EKF provides an improved ego-motion estimate, which helps in estimating the elevation angles of targets, thereby providing a 3-Dimensional localization algorithm, along with a velocity estimator. The height information extracted through this methodology helps in classifying those targets as an object that you can drive under, over or through it. The signal model and algorithm are created and tested through MATLAB and validated on actual radar measurement. A Fully-Integrated 77 GHz Radar Transceiver was used to collect the real data in an outdoor environment [14].

1.5. Outline of the thesis

The structure of the thesis is defined as follows to have an understanding of the flow of information involved in the project.

- **Chapter 2** - The fundamentals of FMCW radar and the signal model will be explained along with a literature overview of the super resolution techniques employed in DoA estimation. The chapter concludes with an insight into the state of the art approaches in height estimation and ego-motion estimation which is a key feature in the algorithm presented.

- **Chapter 3** - Using the literature review, a conclusion has been provided with an efficient design created with the appropriate techniques, obeying the application requirements of the project. A detailed account of the strategy employed and the flow of information shall be discussed in this chapter.

- **Chapter 4** - The signal processing chain is evaluated in the MATLAB simulation environment. The results and the observations shall be analysed and conclusions would be made to support the research questions introduced in this thesis.

- **Chapter 5** - The simulation results are validated by real-time experiments done with the Fully-Integrated 77 GHz Radar Transceiver, provided by NXP Semiconductors, in the premises of Delft University of Technology.

- **Chapter 6** - Chapter 6 finalizes the research studies and recommendations will be provided on the future prospects in this field.

2

Fundamentals of Automotive Radar

In this chapter, an introduction is provided on the various underlying concepts and techniques in automotive radar discussed and utilized during the course of this thesis. To start with, the fundamentals of FMCW is discussed, to provide with a basic understanding on its working principle. The signal model and its configuration discussed taking into account the application of the project. In the following section, an analysis on the state-of-the-art DoA estimation techniques is provided along with multiple height estimation techniques using the existing literature is discussed. This chapter serves as a literature study for the following chapter, to have an understanding on the the reasoning behind the design choices employed in constructing the fast, low-complexity classification algorithm.

2.1. Measurement Parameters

At present, the automotive radar detects targets based on the three parameters such as range, velocity and angle. The range can be determined via the measurement of the delay of the received signal (reflection from the target), velocity calculation done using the Doppler effect property and the angle of targets are determined using more than one transmit or receive channel. Various signal processing techniques are involved in the the accuracy and precision of the estimated parameters to the true value. The resolution factor plays a significant role in being able to resolve targets in all measurement dimensions: range, velocity and angle, which are shown below:

$$\Delta R = \frac{c}{2B} \text{ [m]} \tag{2.1}$$

$$\Delta v = \frac{\lambda}{2T_{\text{frame}}} \text{ [m/s]} \tag{2.2}$$

$$\Delta \theta \approx \frac{0.886\lambda}{(N-1)d\cos\theta} \text{ [deg]} \tag{2.3}$$

where, c is the speed of the light, B is the transmission bandwidth, λ is the wavelength, T_{frame} is frame time, d is the inter-element spacing in the virtual array, and N is the number of of virtual array elements. With d equal to $\lambda/2$, it becomes a Uniform Linear Array (ULA).

2.2. Frequency Modulated Continuous Wave (FMCW) Radar

Radar which stands for ”Radio Detection and Ranging”, is an object detection system that employs electromagnetic wave (radio or micro waves) in detecting and localizing targets. The radar waveforms are mainly classified into two categories, namely, Pulsed Waveform and Continuous Waveform. Pulsed radars transmit pulses of short duration, at regular time intervals. The reflected signal from the target is received in the time intervals between transmissions. The range of the reflected target is calculated from the delay or the time elapsed between the transmission and reception, of the reflected signal. While the pulsed radar systems employs a sequential transmission and reception, Continuous Wave radars transmits a stream of continuous waveform signals i.e. a simultaneous transmission and reception. In CW radars, the velocity of the target can be calculated using the property of Doppler effect, which produces a frequency shift in the reflected signal in comparison to the transmitted signal.

However, to carry out target range estimation, frequency modulation is employed on the transmitted signal which brings us to Frequency Modulated Continuous Wave (FMCW). In FMCW radar utilizing the linear frequency modulated waveform (LFM), the range of the target is calculated from the frequency shift between the transmitted and received signal [15]. The FMCW radars are widely used in the automotive radar systems, aiding safety applications in ADAS such as adaptive cruise control, collision avoidance, parking aid and so on due to various advantages [16]. In comparison to pulsed radars, the advantages of FMCW radar are the low measurement time, low power consumption and cost-effective. Theoretically, unlike the pulsed radar, the FMCW radar do not require signal blanking and can measure targets at short ranges with high accuracy and resolution.

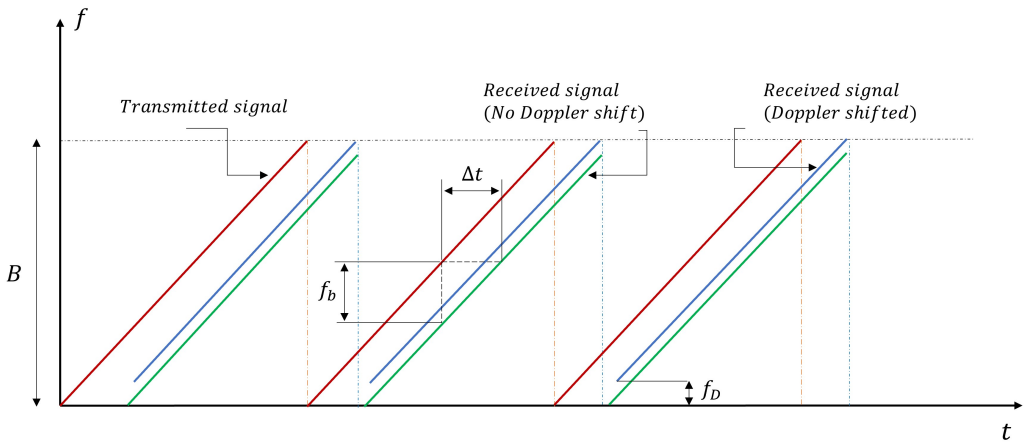

Figure 2.1: Visualization of the FMCW chirp signal

In automotive application, the primary concept of FMCW radar is to generate, as previously mentioned, a linear frequency modulated ramp as transmit signal, also called a chirp. The illustration of the chirp signal is shown in Figure 2.2.

$$s_T(t) = A_t \exp\left\{j2\pi\left(\frac{\alpha}{2}t^2 + f_c t\right)\right\} \tag{2.4}$$

The received signal upon reflection from k targets includes the time delay τ between the transmit and received signal.

$$s_R(t,k) = A_r \exp\left\{j2\pi\left(\frac{\alpha}{2}(t-\tau_k)^2 + f_c(t-\tau_k)\right)\right\} \tag{2.5}$$

where, chirp slope $\alpha = B/T$

B being the bandwidth, T being the chirp duration, f_c being the center frequency and A_t and A_r being the complex amplitudes of the transmitted and received signal.

Upon reception, received signal from the reflection of the target is mixed with the transmit signal. This is called stretch processing (deramp/dechirp), as the received signal is transformed into a sinusoidal form through the mixer and resulting in an IF signal or beat signal.

$$s_{\text{beat}}(t,k) = A_b \exp\left\{j2\pi\left(\alpha\tau_k t - \frac{\alpha}{2}\tau_k^2 + f_c\tau_k\right)\right\} \tag{2.6}$$

This dechirped received FMCW waveform is used for the estimation of range and radial velocity of the targets through FFT. In case of a single object or a target in front of the radar, the frequency spectrum of the IF signal reveals a constant frequency tone, called beat frequency. Similarly multiple objects reveal multiple frequency tones in the frequency spectrum of the IF signal. This beat frequency is the difference between the transmit and received frequency and it is proportional to the range of the object from the radar.

$$s_{\text{beat}}(t,k) = A_b \exp\left(j2\pi\alpha\tau_k t\right) \exp j2\pi\left(f_c\tau_k - \frac{\alpha}{2}\tau_k^2\right) \tag{2.7}$$

The generalized beat frequency representation can be derived, when the value of $\tau_k = 2(R + v \cdot t)/c$, where R and v is the range and relative velocity of the k^{th} target respectively, is substituted in Equation 2.7, given below.

Since $4(R + v.t)^2 << c^2$, $\tau^2 \approx 0$, the last term can be neglected.

$$s_{\text{beat}}(t,k) = \exp\left\{j2\pi\left(\frac{2f_c \cdot R}{c} + \left(\frac{2f_c \cdot v}{c} + \frac{2\alpha \cdot R}{c}\right)t + \frac{2\alpha v}{c}t^2\right)\right\} \tag{2.8}$$

Collecting terms that are linear with t, we find that the beat frequency term contains the range information polluted with doppler.

$$f_{beat} = \frac{2\alpha \cdot R}{c} + \frac{2f_c \cdot v}{c} \tag{2.9}$$

This shows the so-called range-Doppler coupling, where a target at distance R and velocity v is not seen at range bin R, but at a shifted range bin R' due to the effect of the velocity v. With respect to stationary targets, i.e. $\tau_k = 2.R/c$ and subsequently substituting in Equation 2.7, we can see that the $\alpha\tau$ term in the beat signal represents the beat frequency f_{beat} to compute range and the $f_c \cdot \tau$ represents the phase information, which is used for DoA estimation.

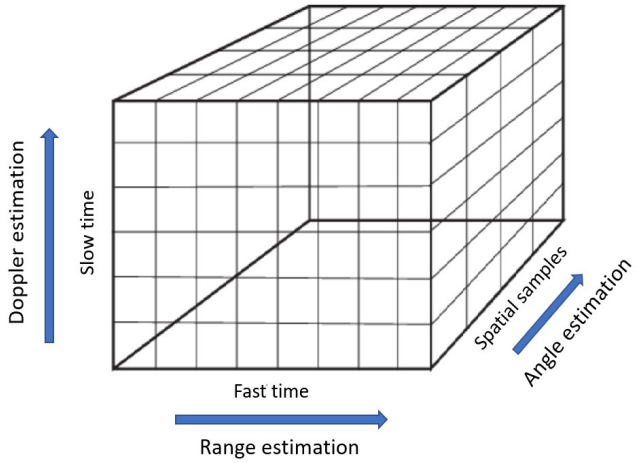

Figure 2.2: Radar data cube

Radar signal processing operates on data that are sampled in more than one dimension, with the idea to extract range, velocity and angle. The radar information collected is stored in a data cube with dimensions being, fast time, slow time and spatial samples as shown in Figure 2.2. As discussed in the previous section, a sequence of chirps (pulses) is being transmitted by the radar and these are received upon reflection from the target. Upon reception, and undergoing stretch processing, the resulting IF signal or beat signal, given in Equation 2.7 is sampled. The collected samples within a pulse or a chirp are referred to as fast time samples. These fast time samples containing the delay of the reflected signal, correspond to successive range intervals and are used to estimate the range of the target through Fast Fourier Transform (FFT). The range samples are also called as range gates or range bins. An important parameter, named PRI (Pulse Repetition Interval) should be introduced, as it determines the number of chirps (pulses) transmitted per second. Due to the long sampling interval of typical PRI's compared to the fast time interval, samples are taken from different pulses. Within the same range gate or range bin, these complex samples collected from different pulses are called as slow time samples. This allows for Doppler processing by means of FFT along the slow time dimension, thereby exploiting the phase difference between chirps to obtain the radial velocity of targets at a given range bin. Hence, on applying the 2-Dimensional FFT, we can see that the peak will appear at a bin, giving the information about the range and velocity of the target that correlates with the terms $[\frac{2 \cdot R}{c}, \frac{2f_c \cdot v}{c}]$, which the beat signal represents, as mentioned in the Equation 2.9. In case of multiple receiver channels or based on number of transmitter receiver pairs, the collected samples representing the reflections from the object at different antenna elements, are stored in the spatial dimension. This dimension is used in the estimation of DoA by means of FFT on the spatial samples corresponding to the range-Doppler bin associated to the target. The phase differences of the received signal between different antenna elements is exploited in determining the DoA of the target. The range resolution as defined in the Section 2.1, depends on the bandwidth of the FMCW waveform and the Doppler resolution depends on the total measurement time and

SNR (Signal-to-Noise Ratio).

To summarize, in case of a single target, upon reception of the reflected signal from the target and demodulation, the radar data is stored in the form of data cube. The range-Doppler processing is carried out for each spatial channel by applying an FFT on the fast time and an FFT on the slow time samples, for instance, in a virtual array of 12 receive (spatial) channels with 3 transmitters and 4 receivers which shall be explained in further in Section 2.3. A single target will be perceived in a range and Doppler bin having more energy. After extracting the spatial samples associated to the target range and Doppler bin, another FFT is performed along the spatial dimension to determine the angle of the target. These extracted samples together constitute a snapshot, which is illustrated in Figure 2.3.

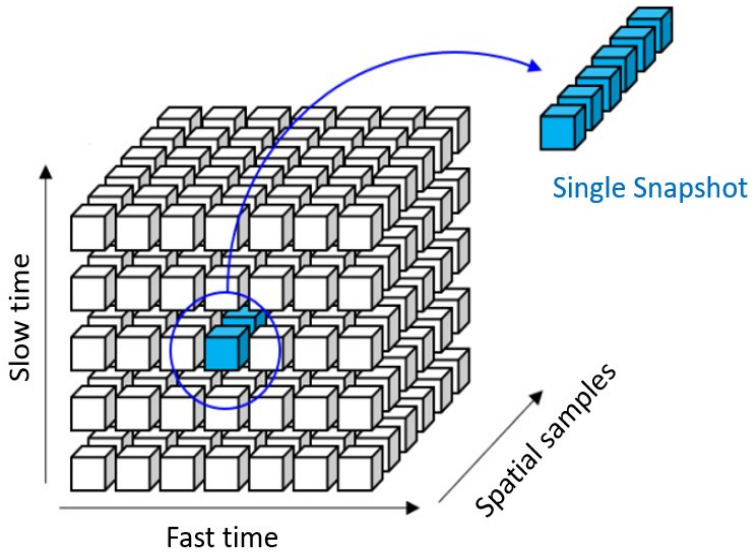

Figure 2.3: Representation of single snapshot extraction after range-Doppler processing [17]

2.3. Signal Model

In this section, we discuss the MIMO (Multiple-Input Multiple-Output) radar. MIMO radar utilizes multiple elements in transmitter and receiver array, giving rise to a larger virtual array. Suppose using M_{tx} transmitters and M_{rx} receiver antennas, one can realize a virtual array of $M_{tx} * M_{rx}$ elements. In this manner, a virtual array of, for example, 16 elements can be realized using 4 transmitter and 4 receiver antennas, which is cheaper than the conventional way of having 1 transmitter and 16 receiver antennas i.e. 17 analog channels, compared to 4 + 4 = 8 analog channels. Hence, MIMO radar provides an improved angular resolution in an efficient way as compared to the conventional radar with a single transmitter. MIMO radar offers waveform diversity at the transmitter (Tx), by the use of multiple antennas to transmit diverse waveforms simultaneously. MIMO radar systems are classified into two categories: widely separated MIMO and collocated MIMO. One providing higher detection performance and the other, giving an improved angular resolution, respectively [18][19]. In this project, we shall focus on the concept of collocated MIMO radar and its application in DoA estimation.

In collocated MIMO radar, the signals transmitted from the multiple transmitters can be separated at the receiver by using orthogonal waveforms. The four common techniques in achieving these are: time division multiplexing (TDM), code division multiplexing (CDM), frequency division multiplexing (FDM) and doppler division multiplexing (DDM). Of the four, the DDM scheme is widely used in automotive radars. These multiplexing schemes supports the creation of mutual orthogonal waveforms for the transmitters, which gives the ability for the receiver array to separate the transmitter signals [20]. The MIMO configuration of multiple transmitter and receiver elements creates virtual position of receiving channels/antenna elements through spatial convolution of transmitter and receiver phase centers, called virtual array [21]. This provides an increase in the effective number of antenna elements compared to the conventional radar, thereby providing an improved angular resolution and

larger virtual array aperture.

Suppose a MIMO radar system with M_{tx} transmitters and M_{rx} receivers giving rise to a virtual array of elements, $N = M_{tx} * M_{rx}$ elements. The inter-element spacing of the virtual array d is a significant parameter. To avoid grating lobes in the beamforming spectrum, the inter-element spacing should be equal to or smaller than half the wavelength λ. Having all inter-element spacings the same, the resulting virtual array is defined as uniform linear array (ULA). To satisfy this condition, we can compute the inter-element spacing of the virtual array by employing the relation between the inter-element spacing of the receiver and transmitter array and number of receiver antennas, given as:

$$d_R = \frac{d_T}{M_{rx}} \tag{2.10}$$

For our application in this thesis, we have employed a a virtual array with 12 elements, where M_{tx} = 3 and M_{rx} = 4. By using the condition in 2.10, we can also achieve the desirable inter-element spacing of $\lambda/2$, by taking $d_T = 2\lambda$ and $d_R = \lambda/2$. We can also note that the angular resolution increases with increase in number of sensors or antenna elements (N), which is validated by the Equation 2.3.

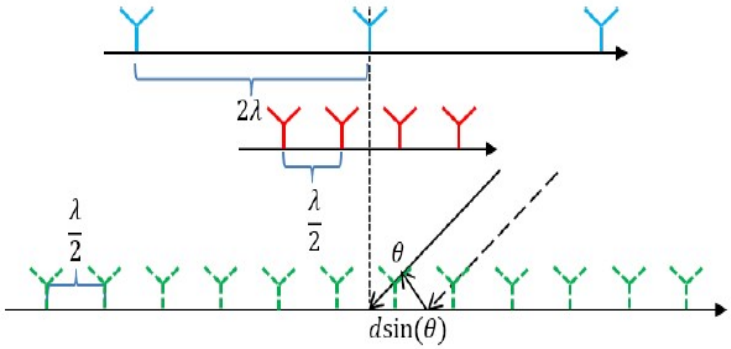

Figure 2.4: Virtual array with 12 elements, the number of transmitter, M_{tx} = 3 and receiver, M_{rx} = 4. The blue solid antennas represent the transmitter elements, and the green dashed antennas represent the virtual elements generated from red receiver antennas [5].

In line of sight (LOS) scenario, the direct path of reflected signal from the target is assumed to be parallel and the delay of the recieved signals is increasing between consecutive elements in the antenna array. Under the narrow band assumption, the delay between the arrival of reflected signals to each antenna element can be translated into phase shifts. The phase shift is increasing linearly in ULA. However, in the case of multipath or non-line of sight (NLOS), the phase shift differs between elements as the direction of departure (DoD) of signals from the transmitter is different from the direction of arrival (DoA) of the reflected signals. In the LOS scenario, the phase difference relative to the N_{th} element is given as:

$$\phi_n = \frac{2\pi(n-1)d\sin\theta}{\lambda} \tag{2.11}$$

where, n = 0,1,...,N-1 with respect to the Figure 2.5.

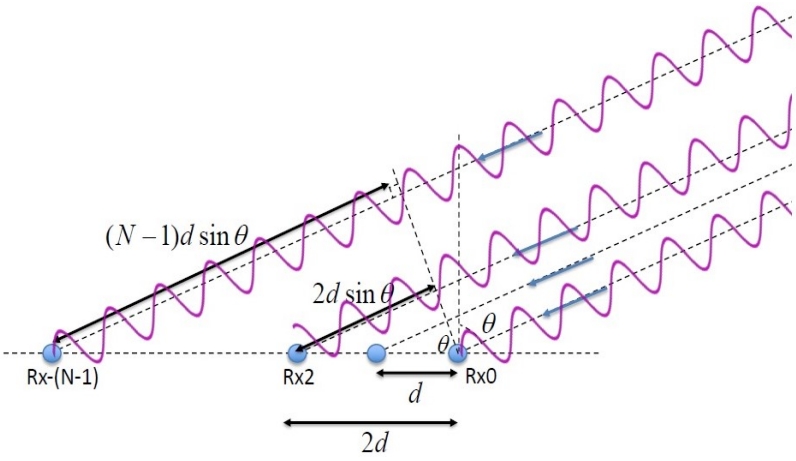

Figure 2.5: Approaching wave-front on the ULA from the target [22]

In LOS scenario, angle of arrival of the target, $\theta_t = \theta_r$ i.e. DoD = DoA. However, in NLOS or multipath scenario, $\theta_t \neq \theta_r$, i.e. DoD $\neq$ DoA. The steering vector representing the reflected signal from the target at an angle θ, indicates the phase delay of each element in the array, $a_T(\theta_t)$ of transmitter array and $a_R(\theta_r)$ of receiver array

$$\mathbf{a}_T(\theta_t) = \left[1, e^{j2\pi \frac{d_T}{\lambda} \sin(\theta_t)}, \ldots, e^{j2\pi(M_{tx}-1)\frac{d_T}{\lambda} \sin(\theta_t)}\right]^T \tag{2.12}$$

$$\mathbf{a}_R(\theta_r) = \left[1, e^{j2\pi \frac{d_R}{\lambda} \sin(\theta_r)}, \ldots, e^{j2\pi(M_{rx}-1)\frac{d_R}{\lambda} \sin(\theta_r)}\right]^T \tag{2.13}$$

where, d_T is the inter-element spacing of the transmitter array and d_R is the inter-element spacing of the receiver array.

The steering vector of the virtual array, $\mathbf{a}(\theta)$ is formed by the Kronecker product, $\otimes$, of the steering vectors of transmitter and receiver array. It represents the signal received from the target present at a DoA angle, θ from the antenna elements in the array. The visualization of the incoming signal is given in Figure 2.5.

$$\mathbf{a}(\theta_t, \theta_r) = \mathbf{a}_T(\theta_t) \otimes \mathbf{a}_R(\theta_r) \tag{2.14}$$

In NLOS scenario, the $\mathbf{a}(\theta)$ in the steering vector includes the information of both DoA and DoD as θ_t and θ_r are different. However, in LOS scenario, the $\mathbf{a}(\theta)$ contains the information of a single angle parameter, i.e. DoA as θ_t and θ_r are equal.

The MIMO signal model for received signals from K targets can be expressed as:

$$\mathbf{x} = \mathbf{A}\mathbf{s} + \mathbf{n}, \tag{2.15}$$

where, $k = 1, ..., K$
In the model definition, $\mathbf{A}$ is the steering matrix of dimension $N \times K$ containing the complex elements in the steering vectors $\mathbf{a}(\theta_k)$, $\mathbf{s}$ is the column vector of dimension $K \times 1$ containing the complex signals, s_k, that arise due to the attenuation of signals and change of phase upon reflection from the targets, K and $\mathbf{n}$ is the noise vector.

For the current MIMO configuration, the sensor receives the snapshot consisting of $M_{tx} \cdot M_{rx}$ i.e. 12 spatial samples. These spatial samples corresponding to the range-Doppler bin of the target is then processed for DoA estimation. Moving forward in this thesis, single snapshot DoA estimation becomes a requirement in the project as the automotive application dealt with in this project should be provided with low latency. From the safety point of view, low latency becomes a key factor in automotive applications as it gives the road user and the driver ample amount of time to react in various scenarios.

2.4. Super Resolution Techniques in DoA Estimation

Previously, in DoA estimation, we estimate the angle parameter through FFT along the spatial axis of the radar data cube, achieving a certain angular resolution. In MIMO radar systems, conventional DoA estimation techniques

can be classified into parametric and non-parametric methods. The parametric techniques include Deterministic and Stochastic Maximum Likelihood, DML and SML, respectively, which achieve good performance in DoA estimation. However, it comes at a cost of high computational complexity and it requires a priori information on the number of targets to guarantee maximum likelihood performance, for example, in a probabilistic fashion i.e. $P(|\hat{\theta} - \theta| < \epsilon) > 90\%$ for a given ϵ and SNR. The non-parametric techniques include the conventional digital beamforming and subspace-based algorithms such as MUSIC and ESPRIT. In this section, a short discussion will be provided on these super resolution algorithms of MUSIC and ESPRIT, that were considered and discuss the challenges faced due to the requirements of the automotive application dealt in this project.

2.4.1. MUltiple SIgnal Classification (MUSIC)

MUSIC algorithm is a spectral estimation technique which works on the principle of decomposition of eigen values [23]. The approach is based on the covariance matrices of the signals. It provides high resolution, accuracy and stability, but it is limited to uncorrelated signals and it is computationally expensive. When it comes to correlated signals or low SNR scenarios, the performance of MUSIC deteriorates [24]. To restore the rank of correlation matrix when signals are highly coherent, there exists decorrelation algorithms such as forward-backward averaging (FBA) and spatial smoothing (SS) [25]. In limited number of snapshots scenario, the estimation of noise covariance matrix becomes difficult, i.e. having only a few measurement bins adjacent to the peak range cells of the target, hence the decrease in performance in such scenarios. Taking snapshots from consecutive measurements (frames) has a negative impact on the latency. Another challenge of MUSIC is that the eigenvalue analysis is used to determine the rank of the signal space and therefore the number of targets, to effectively determine the rank of the correlation matrix. However, this is difficult in practical scenarios.

2.4.2. Estimation of Signal Parameters via Rotational Invariance Techniques (ESPRIT)

Another subspace based DOA estimation technique that was looked upon was the ESPRIT, whose technique relies on a special array structure. After the division of the array of antennas into subarrays or doublets and calculation of correlation matrix, the signal subspaces are computed respectively. As the subspaces are translationally related, there exists a unique non-singular transformation matrix which connects the subspaces of eigen vectors. The DoA estimation is computed through the information of this transformation matrix or rotational operator that maps the signal subspace of one subarray to the other. Hence, ESPRIT exploits an underlying rotational invariance among signal subspaces induced by an array of sensors with a translational invariance structure [26]. It does not require pseudo-spectrum calculation like in MUSIC. However, the main challenge of the algorithm exists in scenarios or applications with limited number of snapshots (single) and unknown number of targets [27].

2.5. Space-Time Adaptive Processing (STAP)

STAP is an adaptive filtering technique, providing an ability in detecting targets obscured by clutter or by jamming in airborne radar systems, conventionally. It exploits the target signal structure, jointly in time (pulses in the slow time) and space (antenna array) to detect the velocity and DoA of the target suppressed by clutter or jamming [28]. However, since space-time adaptive processing is just an extension of adaptive beamforming, the problems related to the latter will exist for STAP as well when estimating the space-time adaptive weights. The low number of data samples (training data) does not help the case in estimating the space-time interference-plus-noise covariance matrix, which is of large dimension. Also, there is an issue of computational load when it comes to the application of STAP [29].

2.6. Ego-motion

As mentioned in Section 1.2, the velocity of the car plays an important role in height estimation techniques making Ego-motion estimation, a crucial aspect of the height classification algorithm. The general methods employed in carrying out the Ego-motion estimation is discussed in this section.

2.6.1. Ego-motion based on other modalities

Through visual odometry, the vehicle motion is estimated by employing feature tracking or feature matching on a sequence of images captured through a camera, which can be categorized as monocular or stereoscopic

[30]. In stereovision, the 3D points are reconstructed using triangulation and point features are located using iterative closest point approach (ICP). On the other hand, the monocular cameras require tracking image features over a number of images. The stereo outperforms monocular visual odometry in most number of cases [31]. Using a trifocal tensor, which incorporates all geometric relationships among three views, the features are related between three images of the same static scene, through which the ego-motion of the vehicle is estimated [32]. A combination of wheel-based odometry and inertial sensors with good GPS reception provides an accurate ego-motion estimation. However, external factors related to the terrain, and imperfections in wheel dimensions can lead to an erroneous measurement. Added disadvantages include, expensive highly accurate gyroscopes, the poor signal-to-noise ratio offered by the accelerometers at low accelerations and effects of extensive drift on the respective measurement.

2.6.2. SLAM-based ego-motion

At first, a landmark-based global navigation system was present where artificial landmarks are placed strategically at a test site and its global locations are noted using a radar sensor and its position relative to the radar sensor. Through Kalman filter, the radar range and position measurements noted are fused with vehicle control signals [33]. Upon further expansion to with natural features, Simultaneous Localization and Mapping (SLAM) was used where, the position measurements of the radar system are probabilistically fused with the modeled vehicle motion [34]. Without the knowledge of global positions, the features are identified through the polarization of the reflected radar signal. However, in each scan certain retrievable landmarks are required. Added to that, the approach deals with occlusion, moving targets and clutter targets in each scan. In high speed, it is impossible to provide a reliable result as one landmark is only confined to a limited number of frames. Instead of sparse landmarks, a detailed map was used through a scan matching approach in another SLAM application using a 360° radar sensor. Through scan correlation, a maximum likelihood alignment is computed between two sets of sensor data through which a trajectory of the vehicle can be estimated [35]. However, the disadvantages with the approach include a complex time dependant signal processing and an initialization period.

2.6.3. Radar-based ego-motion

The increase in use of Doppler radars and measurement accuracy offered in the automotive field has opened doors for multiple possibilities for a fast and reliable ego-motion estimation. It is based on the relative motion of the ego-vehicle with respect to stationary targets i.e. the ego-motion is based on the Doppler velocity and azimuth angle of the measured targets in the field of view (FoV) [9]. The movement or the trajectory of the radar sensor can be computed by examining the sinusoidal progress of the radial velocities of the measured stationary targets over their positions in the azimuth angle domain, also called as the velocity profile. By analyzing the velocity profile using a least-square (LS) approach and single-track model with the Ackermann condition, the ego-motion of the vehicle can be estimated [8]. The Ackermann condition mentioned, states that the extended rotational axes of all wheels of a vehicle intersect at one point. The properties of the ego-motion estimation include a time-independent signal processing without any initialization period and high sampling rate. Unlike the measurements based on Section 2.6.1, it is free of bias, drift and does not take into account the interaction of the vehicle to the ground while estimating a 2-D motion state of the vehicle. Furthermore, the added derivation of velocity by changing position over two or more successive frames in visual odometry can be avoided as Doppler radars are able to measure relative velocities of stationary targets in a single measurement.

2.7. Kalman Filter

Kalman filter is a recursive estimation algorithm that can be used for target tracking in localization and navigation systems [36][37]. In this section, the working of the Kalman filter will be discussed and to do so, a 1-Dimensional constant velocity model with x_n being the location at time instant, n, $\dot{x}_n$ being the velocity at time n and Δt being the time steps, is assumed as shown in Equation 2.16.

$$\begin{aligned} x_{n+1} &= x_n + \Delta t \dot{x}_n \\ \dot{x}_{n+1} &= \dot{x}_n \end{aligned} \tag{2.16}$$

One of the major challenges in tracking systems is to provide an accurate and precise estimate of the states of the target i.e. range and velocity in this model, in the presence of uncertainty. The uncertainty in measurement from the GPS receivers or radar arises from the external factors such as thermal noise, changes in satellite positions,

atmospheric effects and so on. The Kalman Filter produces estimates of state variables based on uncertain measurements and helps in predicting the future system states based on past estimates.

As previously mentioned, the two equations presented above represents the dynamic model of a system with constant velocity motion where, x_n represents the range of the target at time instant n and $\dot{x}_n$ represents the velocity of the target at time instant n. Δt represents the time-elapse between two instants. The model in Equation 2.16 assumes zero acceleration. For advanced tracking, constant acceleration model can be also applied. However, this is outside the scope of this project.

To summarize, the process of Kalman filter revolves around three important operation blocks: Predict, Measure and Update. The Kalman filter computations are based on five equations: two prediction equations, two update equations, and Kalman gain equation, which shall be explained in further below.

- **Prediction Block**

  From the dynamic model in Equation 2.16, a prediction of the state i.e. range, assuming a constant velocity can be made. As part of the prediction process, the two equations involved are the state extrapolation equation and covariance extrapolation equation, where the former is shown in the Equation below.

$$\hat{\boldsymbol{x}}_{n+1,n} = \begin{bmatrix} \hat{x}_{n+1,n} \\ \hat{\dot{x}}_{n+1,n} \end{bmatrix} = \begin{bmatrix} 1 & \Delta t \\ 0 & 1 \end{bmatrix} \begin{bmatrix} \hat{x}_{n,n} \\ \hat{\dot{x}}_{n,n} \end{bmatrix} + \begin{bmatrix} 0 \end{bmatrix} [\mathbf{u}_n] + [\mathbf{w}_n] \tag{2.17}$$

$$\hat{\boldsymbol{x}}_{n+1,n} = \boldsymbol{F}\hat{\boldsymbol{x}}_{n,n} + \boldsymbol{G}\boldsymbol{u}_n + \boldsymbol{w}_n \tag{2.18}$$

  where, $\boldsymbol{F}$ is the state transition matrix, $\boldsymbol{G}$ is the control matrix, $\boldsymbol{u}_n$ is the control variable and $\boldsymbol{w}_n$ is the process noise at time instant, n.

  This equations takes care of the prediction or estimation of the future state, based on the known present estimation. The covariance extrapolation equation shown below provides the measure of uncertainty in our prediction.

$$\boldsymbol{P}_{n+1,n} = \boldsymbol{F}\boldsymbol{P}_{n,n}\boldsymbol{F}^T + \boldsymbol{Q} \tag{2.19}$$

  where, $\boldsymbol{P}_{n,n}$ is the covariance matrix at time instant n and $\boldsymbol{Q}$ is the process noise matrix. The process noise incorporates the uncertainty in the dynamic model, which includes the random changes in acceleration during sudden maneuvers i.e. factors affecting the target motion. The value of process noise variances has an impact on the performance of the Kalman Filter as a smaller value can create a lag in estimations when compared to the true value and a higher value can make the Kalman filter create a measurement bias and produce noisy estimations.

- **Measurement Block**

  The predicted value of the states is then compared with the measured value of the states, for instance, the radar measurement. The Equation 2.20, represents the state update equation for the measurement block, where $\boldsymbol{z}_n$ represents the measurement. It produces updated estimates the states i.e. range and velocity, based on the present measurement and known past estimation, under the assumption of zero acceleration of the dynamic model represented by Equation 2.16. The term $(\boldsymbol{z}_n - H\hat{\boldsymbol{x}}_{n,n-1})$, is called as the measurement update $\boldsymbol{y}_n$, where $\boldsymbol{z}_n$ is the actual measurement and $\hat{\boldsymbol{x}}_{n,n-1}$ is the predicted measurement.

$$\hat{\boldsymbol{x}}_{n,n} = \hat{\boldsymbol{x}}_{n,n-1} + \boldsymbol{K}_n \left(\boldsymbol{z}_n - \boldsymbol{H}\hat{\boldsymbol{x}}_{n,n-1}\right) \tag{2.20}$$

  where, $\boldsymbol{H}$ is the observation matrix whose purpose is to convert system state (inputs) into outputs (measurements) using linear transformations.
  Kalman Gain equation, represented by $\boldsymbol{K}$ in the above update equation, is a weighting parameter for the measurement and past estimations, in estimating the current system state. It can be computed through the following equation:

$$\boldsymbol{K}_n = \boldsymbol{P}_{n,n-1}\boldsymbol{H}^T \left(\boldsymbol{H}\boldsymbol{P}_{n,n-1}\boldsymbol{H}^T + \boldsymbol{R}_n\right)^{-1} \tag{2.21}$$

where, $\boldsymbol{R}_n$ is the measurement noise covariance matrix. In the case of radar measurement, the uncertainty in the measurements depends on parameters such as SNR, beamwidth, bandwidth and so on.

- **Update Block**

  As part of the update process, the two equations involved are the aforementioned state update equation and the covariance update equation. The covariance update equation, shown below, measures the uncertainty in the estimation.

$$\boldsymbol{P}_{n,n} = (\boldsymbol{I} - \boldsymbol{K}_n \boldsymbol{H})\, \boldsymbol{P}_{n,n-1} \tag{2.22}$$

  where, $\boldsymbol{K}_n$ is the Kalman gain at time instant n.

  If there is an error or a discrepancy with respect to the measurement block, then the predicted parameters of the states are updated to account for this error to produce a precise value of the current state.

Through repeated iterations, in the presence of uncertainity, more precise and accurate estimation of the states can be made. Kalman filter provides consistent performance in linear systems.

However, as radar provides us with distance, radial velocity and angular measurements in polar coordinate systems and and the Kalman filter has its state in cartesian coordinate system, there is a non-linear relation between measurements and state. Therefore, default Kalman filter can't be used and the so-called Extended Kalman filter (EKF) has to be used.

$$\boldsymbol{x}_{n+1} = f(\boldsymbol{x}_n, \boldsymbol{u}_n) + \boldsymbol{w}_n \tag{2.23}$$

In EKF, the non-Linear functions are made linear through approximation using the linear term in the Taylor series which is related to the 1st derivative of the function that is linearized, called Jacobian Matrix ($\boldsymbol{H}_j$).

$$\boldsymbol{y}_n = \boldsymbol{z}_n - h\left(\boldsymbol{x}_{n-1}\right) \tag{2.24}$$

where, $h\left(\boldsymbol{x}\right)$ is a function that specifies the required mapping of the measurements from one coordinate system to another, i.e. in radar measurements, between Cartesian coordinates and Polar coordinates. In addition, $\boldsymbol{H}$ is replaced with $\boldsymbol{H}_j$ in all further equations of a Kalman filter.

2.8. Height Estimation Techniques

To create a 3-Dimensional localization map of objects in the vehicle surroundings, the task of determining the height of targets plays a significant role, which also is crucial in the safety of autonomous driving. In this section, two methodologies in height estimation are presented.

2.8.1. Multipath Height Finding

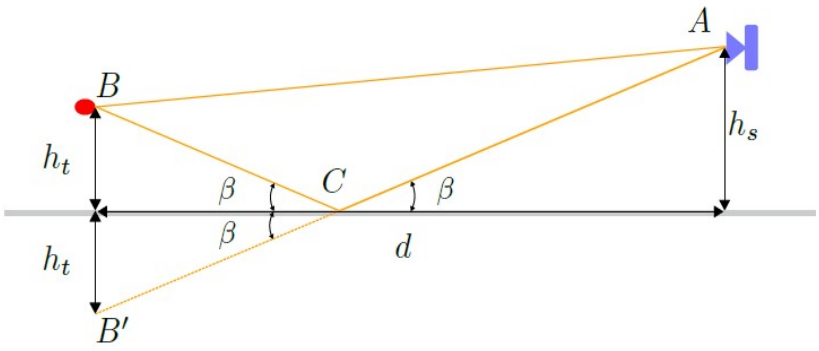

Figure 2.6: Multi-path propagation model used in the height estimation technique [38]

The following height estimation technique determines the height of the target using the multi path properties of the reflected signal [38]. In this technique, the operation is based on the assumptions that the ground is flat and the height of the radar sensor from the ground is known. From the Figure 2.6, the multipath propagation model of the radar signal can be illustrated. Assuming the ground is flat, there are two propagation paths to be noted. One being the direct path (AB) i.e. a LOS scenario and the other is the indirect path (ACB), which is reflected from the ground at point C, i.e. a NLOS scenario. The radar receives the reflected signals from the target through these paths.

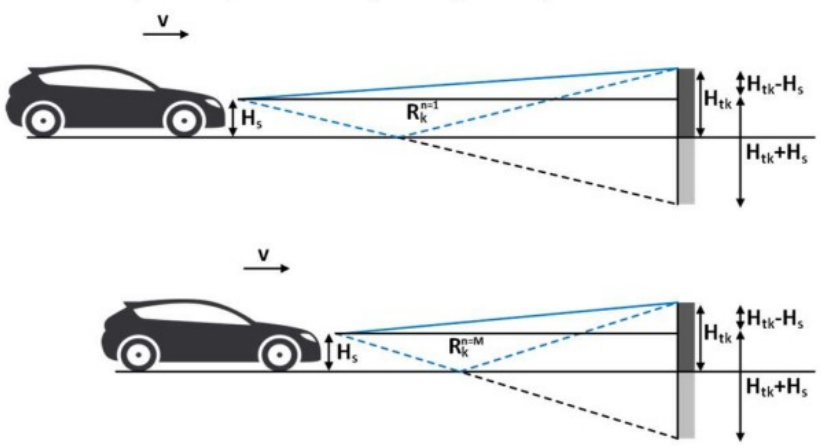

Figure 2.7: Geometry used in derivation of target height [39]. **Top**: Frame n =1; **Bottom**: n = M
Direct path - solid blue line and Indirect path - dotted blue line

Using geometry in Figure 2.7 representing a target at broadside ($\theta = 0°$), and a time reference (in terms of frame number) represented by the superscript, n, the height of the target H_{tk} can be formulated, with the known information of the radar sensor height from the ground H_s. For explaining the concept, two paths are considered i.e. the radar sensor receives the backscattered signal from the target k through a direct path (DP – solid blue line) and an indirect path (IP – dotted blue line) as shown in Figure 2.7. The range of the DP (R_{DP}) and IP (R_{IP}) are given as:

$$\begin{aligned} R_{DP}^n &= \sqrt{(H_{tk} - H_s)^2 + (R_k^n)^2} \\ R_{IP}^n &= \sqrt{(H_{tk} + H_s)^2 + (R_k^n)^2} \end{aligned} \tag{2.25}$$

Using the range information,

$$H_{tk} = \frac{(R_{IP}^n)^2 - (R_{DP}^n)^2}{4H_s} \tag{2.26}$$

Using Taylor expansion and replacing the ground distance d with radial distance R_{DP}, the Equation 2.26 can be further approximated to the following [38]:

$$H_{tk} \approx \frac{\Delta r R_{DP}^n}{2H_s} \tag{2.27}$$

where, Δr represents the range difference information between the direct path and indirect path.

However, in this technique, the means by which the direct path and indirect path is differentiated is through the difference in the amplitude of the spectral peaks in the range domain. The highest amplitude peak is selected as direct path or LOS component and the highest amplitude peak with range further than the direct peak's range is considered as the indirect path or multipath or NLOS component. However, ideally either one or two spectral peaks in the range domain are expected, but in practice, there can be much more additional peaks originating from the diffuse scattering from rough surfaces and reflections from other parts of the target, which can create ambiguities and make the selection of LOS component difficult.

2.8.2. Vertical Doppler Beam Sharpening

In this technique, the height is determined by relying on the doppler frequency shift induced by the target's velocity relative to the radar. The relative velocity detected by the radar with respect to the stationary objects depends on the elevation and azimuth angle of the object.

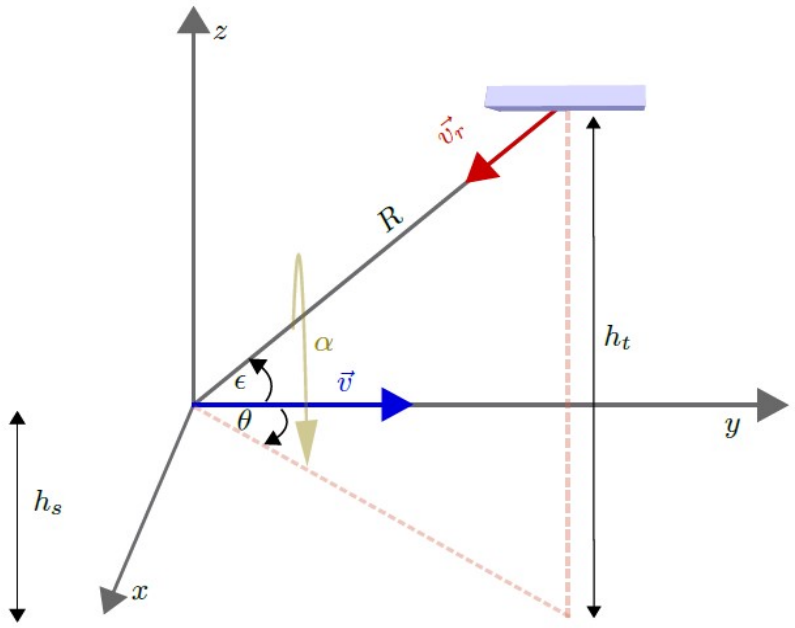

Figure 2.8: Geometry employed for height estimation using Doppler Beam Sharpening [40]

From the Figure 2.8, assuming the car driving with velocity, v in the y-direction towards a stationary target of height h_t, the radar receives a detection with range R, radial velocity v_r and angle θ. Hence, the radial velocity formulation is computed as shown below:

$$v_r = -v\cos\alpha \tag{2.28}$$

where, α contains the information of the azimuth (horizontal) and vertical angle (elevation) component of the target.

Furthermore, in expanding and deriving the radial velocity component $v_{r_{el}}$ dependent on the elevation angle, ϵ can be given as:

$$v_{r_{el}} = -v\cos(\epsilon) = \frac{v_r}{\cos(\theta)} \tag{2.29}$$

Using the geometry, the height of the target, h_t is calculated as:

$$h_t = h_s + R\sin\epsilon = h_s + R\sin\left(\arccos\left(-\frac{v_{r_{el}}}{v}\right)\right) \tag{2.30}$$

where, R is the measured range of the target.

The high accuracy in the height estimation of targets using this technique, has been documented [40]. Unlike the multipath height finding, this technique does not require a separate detection and classification of direct and indirect path, in terms of range information, before proceeding into the height estimation procedure. From the above equation, the effect of the ego-velocity in height estimation can also be seen, where the error in ego-velocity can alter the height estimation, thereby providing an unreliable 3-D localization of targets.

2.8.3. Conclusion

In this chapter, the fundamentals of the automotive radar and the techniques involved in the estimation of measurement parameters are discussed. The FMCW radar employed in the automotive radar systems is studied and the equations are presented in detail, which are used to estimate the range and DoA of the target. Subsequently, the MIMO radar signal model for a target is presented and discussed along with a brief overview of the range-Doppler processing with respect to the radar cube for a FMCW waveform. After the range-Doppler processing, the DoA estimation is to be conducted, for which a short discussion is provided on multiple DoA estimation techniques for instance, the super resolution techniques such as MUSIC and ESPRIT. Through the discussion, it is shown that the super resolution techniques has its disadvantages in single snapshot estimation scenarios. However, a DoA estimation using single snapshot is needed and to be looked at for a quick response automotive radar system. A short discussion is also provided on the methods employed in carrying out the ego-motion estimation detailing the state-of-the-art and the challenges it faces. Through the discussion, the dependance of Dopper velocity and azimuth is seen in the radar based ego-motion methodology. However, the focus of this project is to remove the bias and add the elevation angle factor in the ego-motion estimation technique, which shall be discussed in further, in the documentation. The application of Kalman Filter in target tracking is discussed along with equations to provide a rudimentary understanding on its operation. Two methodologies in height estimation are presented showcasing the difference in two approaches and an idea of how it can be implemented or used in the application of the proposed algorithm.

3

Signal Processing Chain

This chapter introduces the height classification algorithm explaining the flow of information through the different stages. Adhering to the application requirements, a methodology has been chosen which shall be explained in this chapter.

3.1. Application Specifications

In developing an efficient and low-complexity localization algorithm, certain specifications i.e. assumptions and requirements were taken into account. The targets dealt with are assumed to be stationary in this model and the antenna configuration is oriented in such a manner to incorporate the azimuth angle domain and does not cover the elevation angle domain, enabling a better performance in detection in the azimuth.

Low latency parameter (range, velocity, DoA) estimation is an important requirement in automotive applications due to the safety requirements, as it enables the user or automobile to act quickly in emergency situations. For DoA estimation, this is achieved by using a technique based on single snapshot, i.e. for every detected target, one estimation per radar frame. The lack of time integration for the estimated parameters is compensated by tracking algorithms that do averaging and consistency checks.

3.2. DoA Estimation

As discussed in Section 2.2, in FMCW radar systems, the beat signals convey range and angle information. This enables us to employ joint parameter estimation techniques such as 2-D MUSIC, 2-D ESPRIT to estimate the azimuth/elevation and range of targets [41]. However such techniques increases the computational load which is not desirable in real-time FMCW automotive radar systems. Furthermore, taking into account the aforementioned application requirements, MIMO-Monopulse was chosen to carry out the DoA estimation of the targets i.e. by combining the monopulse approach with MIMO radar [5]. The application of monopulse in MIMO collocated radar is discussed in [42].

Monopulse is a fast and accurate angle estimation technique well developed for target tracking. The advantage of the monopulse technique is to be able to work with a single snapshot for DoA estimation and is computationally less expensive compared to the other DoA estimation techniques mentioned in Section 2.4. In tracking, usually analog beamforming is used and 2 beams (or 4 beams) are put on the target to be tracked. The two types of monopulse radar are phase comparison monopulse and amplitude comparison monopulse radar.

Amplitude comparison monopulse can be realised in a conventional monopulse system consisting of two identical antennas at the same phase center with a squint angle, whose outputs are subtracted to produce a difference beam and summed up to produce a sum beam as shown in Figure 3.1a. It compares the voltages of the receiving beams which differ by a squint angle, simultaneously with an overlapping pattern on the main direction. The idea of the amplitude comparison monopulse is that for every direction of arrival, the difference in the amplitude of the received signal will be a measure for angular displacement [43].

Similarly, phase comparison monopulse can be realised in a conventional monopulse system consisting of two identical antennas, seperated by a certain distance as shown in the Figure 3.1b. Furthermore, more antennas can be used for getting more robust estimation, where the certain distance has to be less than or equal to $\frac{\lambda}{2}$ for atleast one pair of antennas. The idea of the phase comparison monopulse is that angle of arrival is computed using the phase difference measurement between the two received signals from the target due to the angular position of the object, received by the two different channels.

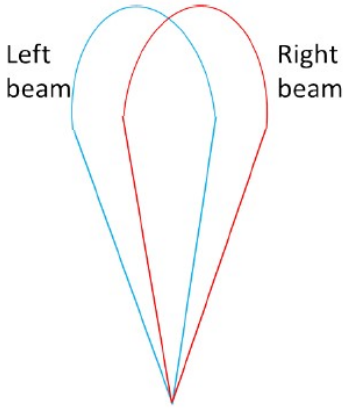

(a) Amplitude Comparison approach

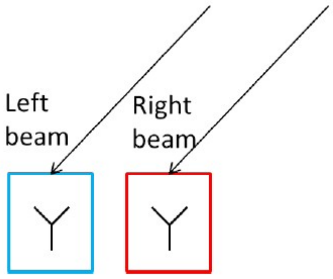

(b) Phase Comparison approach

Figure 3.1: Classification of Monopulse radar [44]

In our application we use digital beamforming and use beamforming spectrum to find 2 consecutive ”beams” that ”illuminate” the target. The 2 beams are the 2 FFT bins if we use FFT for calculating the beamforming spectrum, which shall be explained further below. Furthermore, Phase Comparison Monopulse (PCM) can be implemented directly on the snapshot, and Amplitude Comparison Monopulse (ACM) after FFT (beamforming) of the snapshot. Provided that targets are sufficiently separated in DoA domain, ACM can be used to estimate multiple targets per snapshot. With PCM, the technique is limited to single target per snapshot. Amplitude comparison technology is widely used due to its straightforward design and minimal equipment requirements .

3.2.1. MIMO-Monopulse

Unlike the classical monopulse or phased array monopulse approach, in MIMO-Monopulse technique, the virtual array is utilized to synthesize monopulse beams, which takes the advantage of both transmit and receive array elements. Using the virtual array of the collocated MIMO radar, the sum and difference beams are generated through digital beamforming (DBF) to estimate the angle of arrival of a target at a particular direction [44]. For a received signal, the output of the beamformer can be expressed as:

$$y = \mathbf{w}^H \mathbf{x} \tag{3.1}$$

where, $\mathbf{w}$ is the beamforming vector, obtained through beamforming algorithms such as Bartlett or Capon and $(.)^H$ is the Hermitian operator (complex-conjugate transpose) and $\mathbf{x}$ is the signal to be processed.

Under the far-field assumption, the wave incident on the array is planar. Considering a ULA with N antenna elements, the received plane wave at n-th antenna element characterized by a reflection coefficient A and a DoA angle θ of a single source can be expressed as:

$$x_n(t) = a(\theta) A s_0\left(t - T_n\right) e^{-j2\pi f_c T_n} \tag{3.2}$$

where $a(\theta)$ is the gain pattern and is assumed to be the same for all antennas in ULA.

Defining $s(t) = s_0\left(t - T_1\right), \tau_n = T_n - T_1$, and $\beta = Ae^{-j2\pi f_c T_1}$, where T_n is the propagation time to the n-th element, results in the below Equation:

$$x_n(t) = a(\theta)\beta s\left(t - \tau_n\right) e^{-j2\pi f_c \tau_n} \tag{3.3}$$

Furthermore, using the narrow band assumption, i.e. τ_n smaller compared to the inverse bandwidth of $s(t)$, $s_{\tau_n}(t)$:= $s\left(t - \tau_n\right) e^{-j2\pi f_c \tau_n}$ can be equated to $s\left(t\right) e^{-j2\pi f_c \tau_n}$. The above Equation 3.3 can then be written as:

$$x_n(t) = a(\theta)\beta s\left(t\right) e^{-j2\pi f_c \tau_n} \tag{3.4}$$

where, time delay, $\tau_n = \frac{(n-1)d\sin\theta}{c}$ and $n = 1, 2, 3, ..., N$.

Collecting all the received signals into a vector **x**, results in the data model of the form given as:

$$\mathbf{x}(t) = a(\theta)\beta \begin{bmatrix} s_{\tau_1}(t) \\ s_{\tau_2}(t) \\ \vdots \\ s_{\tau_N}(t) \end{bmatrix} = \begin{bmatrix} 1 \\ e^{-j2\pi f_c \tau_2} \\ \vdots \\ e^{-j2\pi f_c \tau_N} \end{bmatrix} a(\theta)\beta s(t) := \mathbf{a}(\theta)\beta s(t) \tag{3.5}$$

where, $\mathbf{a}(\theta)$ is the array response vector or the steering vector of the signal. Furthermore, the gain pattern, $a(\theta)$ is generally omitted by assuming omnidirectional antennas with unity gain. The following expression is the noise-less response for a single target, in practice, there is additive noise.

Considering a single unit amplitude signal i.e. $|\beta s(t)| = 1$, arriving from a DoA angle θ_0, given as:

$$\mathbf{x}(t) = \mathbf{a}(\boldsymbol{\theta_0})\beta s(t) \tag{3.6}$$

Substituting the aforementioned beamforming vector, **w** i.e. $\mathbf{w} = \mathbf{a}(\theta)$ over all values of the theta ranging from $-\pi$ to π, and the above signal parameter in the Equation 3.1, the output power of beamformer can be computed as follows:

$$|y(t)| = \left|\mathbf{w}^{\mathrm{H}}\mathbf{a}(\theta_0)\right| \tag{3.7}$$

In summary, using DBF, DoA estimation can be realised by searching the maximum of the DBF response pattern at the direction of the steering vector, which can be defined as [44]:

$$P(\theta) = \mathbf{w}^H \mathbf{a}(\theta_0) \tag{3.8}$$

where, $\mathbf{a}(\boldsymbol{\theta_0})$ is the steering vector of the received signal and **w** is the aforementioned beamforming vector.

The amplitude comparison monopulse utilizes DBF algorithm to generate the difference and sum beam. The ratio of difference to sum beamforming output, called as monopulse ratio, can be computed to the determine the DoA of the target.

3.2.2. Amplitude Comparison Monopulse (ACM)

In amplitude comparison monopulse, the approach taken is to generate the left and the right beams using two beamforming vectors centered at a look direction θ_0, seperated by a squint angle θ_s to left and right respectively. Using the MIMO virtual array of M elements and definition of steering vector given in 2.12, the ACM weights of the two beamformers corresponding to the left (l) and right (r) beams, can be expressed as:

$$\begin{aligned} \mathbf{w}_l &= \mathbf{a}\left(\theta_0 - \theta_s/2\right) \\ \mathbf{w_r} &= \mathbf{a}\left(\theta_0 + \theta_s/2\right) \end{aligned} \tag{3.9}$$

where, $\mathbf{w}_l$ and $\mathbf{w}_r$ are Bartlett beamforming vectors.
Furthermore, the sum and difference weight vectors, are expressed as:

$$\begin{aligned} \mathbf{w}_\Delta &= \mathbf{w}_l - \mathbf{w}_r \\ \mathbf{w}_\Sigma &= \mathbf{w}_l + \mathbf{w}_r. \end{aligned} \tag{3.10}$$

where, Δ and Σ represent the difference and sum.

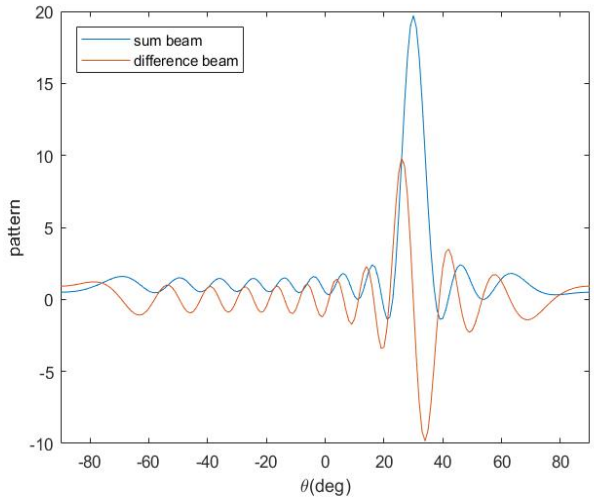

Figure 3.2: Real part of sum and difference beam

After beamforming using the vectors given above, the beamformer output of the sum and difference beams is compared to localize the angle of the target. When the radar scans over the target, if the target is present exactly in the look direction θ_0, then the difference beam output will be zero and the corresponding sum beam output will be maximum. The Figure 3.2 shows the real part of sum and difference beam. The comparison is made using the monopulse ratio, which is defined as the ratio of the difference to sum beamforming outputs. When the target is not exactly in the look direction θ_0 i.e. having a small offset angle $(\theta - \theta_0)$, the output of the difference beam results in an ”error voltage”, which can be defined as the real part of the monopulse ratio.

$$\epsilon = \Re\left\{\frac{\mathbf{w}_\Delta^H \mathbf{x}}{\mathbf{w}_\Sigma^H \mathbf{x}}\right\} \tag{3.11}$$

where, ϵ represents the ”error voltage” and $\mathbf{x}$ is the received array response.

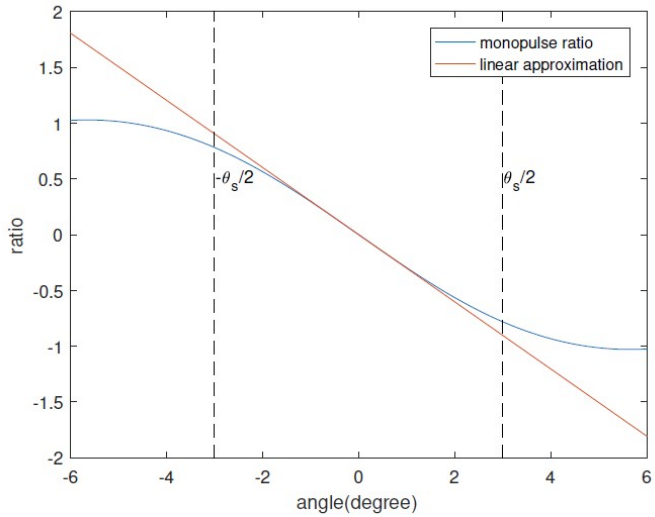

Figure 3.3: Monopulse ratio [5]

Once an error voltage is present, it can be used in conjunction with an ideal monopulse ratio resulting in an monopulse response curve (MRC) to arrive at an angle estimate $\hat{\theta}$ close to the true azimuth of the target, θ. An ideal monopulse ratio is defined as the real part of the ratio of difference to sum responses with the angle to be estimated, which is given by:

$$\Re\left\{\frac{\mathbf{w}_{\Delta}^{H}\mathbf{a}(\theta)}{\mathbf{w}_{\Sigma}^{H}\mathbf{a}(\theta)}\right\} \tag{3.12}$$

Furthermore, a linear approximation of the monopulse ratio is carried out in a local region around the looking direction. The target angle is then estimated, as shown below, through linear mapping the error voltage using the constant slope of the linear approximation, which is given by γ.

$$\theta_T = \theta_0 - \gamma^{-1}\epsilon \tag{3.13}$$

where, θ_T is the final DoA estimate of the target.

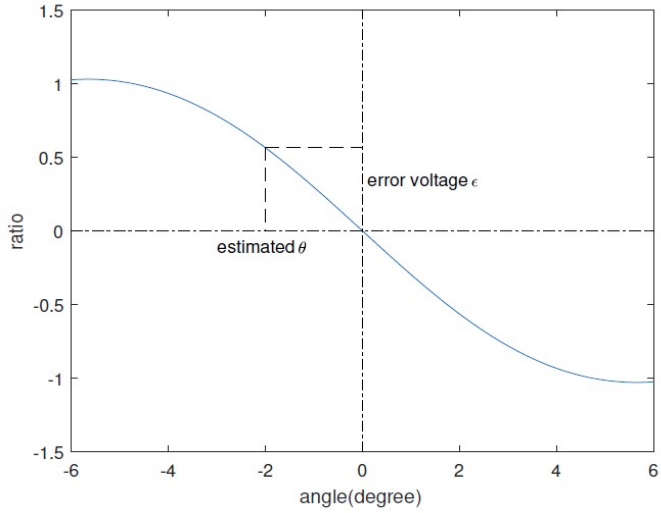

Figure 3.4: Inverse mapping the error voltage [5]

Therefore, for a given error voltage measurement, the target DoA can be determined by inverse mapping the error voltage through the monopulse response curve (MRC).

Moreover, a trade-off exists when it comes to choosing a value of the squint angle. A small squint angle leads to a sharp monopulse ratio but a narrow linear region for tracking the target. On the other hand, a large squint angle leads to a distortion of sum beam pattern. Usually, the -3dB point of the beam is chosen as the squint angle.

3.2.3. Phase Comparison Monopulse (PCM)

In phase comparison mononpulse, as the name suggests, the phase information is employed to compute the angle measurement. Using the MIMO configuration, the virtual array of N elements is divided into two sub arrays, the left sub-array consisting of $\frac{N}{2}$ elements and the rest of the elements constituting the right sub-array [45]. The left and the right beams are generated by the two sub arrays and the left and right beamforming vectors of length $\frac{N}{2}$ are respectively defined as $\mathbf{w}_l$ and $\mathbf{w}_r$. Unlike the amplitude comparison monopulse, the left and the right beam pattern have almost similar amplitude at the looking direction θ_0, but a different phase between the two subarrays. This difference in the phase information is used to determine the target angle. The phase difference between the left and right beam is zero, when the target is located exactly in the look direction of the beam. The sum and difference beamforming outputs are defined as:

$$\begin{aligned} P_\Delta(\theta) &= \mathbf{w}_l^H \mathbf{a}_l(\theta) - \mathbf{w}_r^H \mathbf{a}_r(\theta) \\ P_\Sigma(\theta) &= \mathbf{w}_l^H \mathbf{a}_l(\theta) + \mathbf{w}_r^H \mathbf{a}_r(\theta) \end{aligned} \tag{3.14}$$

where, $\mathbf{a}_l$ and $\mathbf{a}_r$ are the steering vectors of the two sub arrays respectively and $\mathbf{w}_l = \mathbf{a}_l(\theta_0)$ and $\mathbf{w}_r = \mathbf{a}_r(\theta_0)$.

The monopulse ratio, in a similar fashion, is represented as the ratio of the difference to sum beamforming outputs. However, unlike amplitude comparison monopulse, the imaginary part of the monopulse ratio is taken as ”error voltage” in the process of DoA estimation. The linear approximation of the imaginary part of the monopulse ratio, which is a tangent function, is done around the looking direction [5].

3.3. Multipath distinction

In height classification, the detections of the indirect path along with the direct path of the reflections from the target holds a significant value as it helps in the association of the detections to the respective target. Furthermore, it can also be used as a reference in traversability conditions for an algorithm [39]. In scenarios where the DoA is not equal to DoD, i.e. indirect path/multipath, an approach using phase comparison monopulse was taken into account. Using the phase information of the virtual antenna element pairs, the indirect paths can be differentiated. As discussed in Section 2.12, in the virtual array consisting of M_{tx} transmitters and M_{rx} receivers, one has elements that belong to the same transmitter (Tx) and different receivers (Rx). The DoA information lies in the phase difference between these elements and it can be used to estimate the DoA of a single target. On the other hand, there also exists elements falling under a different transmitter (Tx) and same receivers (Rx). Similarly, the DoD can be calculated by utilizing the phase information between these elements. The representation of the aforementioned process using the antenna configuration is shown in the Figure 3.5.

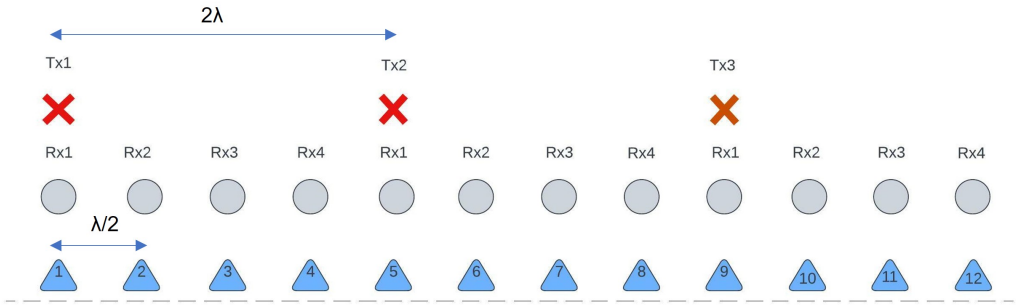

Figure 3.5: MIMO model having a virtual array of 12 elements with 3 Tx and 4 Rx

Corresponding to the Figure 3.5, in DoA estimation, the phase difference between antenna element pairs 2-1, 3-2, 4-3, 6-5,...12-11 is considered, whereas in DoD estimation, the phase difference between antenna element

pairs 5-1, 6-2, 7-3,....12-8 is considered.

For instance, in DoA calculation, consider the antenna elements 1 and 2. The phasor is calculated by multiplying the complex responses of the antenna elements i.e. $A_2 * A_1^H$ where the angle of the result provides the phase difference. In a similar fashion, with the rest of the aforementioned antenna elements, their respective phasors can be calculated. At the end of the calculation of the phasor of final antenna element pair, the following phasor can be summed up to get a robust estimate of the phase difference. Substituting the resulting value in the Equation 3.15, we get an estimate of the DoA.

$$\theta = \text{asin}\left(\frac{\phi\lambda}{2\pi d}\right) \tag{3.15}$$

where d is the distance between the respective antenna element pair i.e. $\lambda/2$ between 2 Tx and $\lambda/2$ between 2 Rx.

The calculations can be repeated for estimating the DoD by using the associated antenna element pairs.

Exploiting the phase differences between virtual antenna element pairs, a robust estimator of DoA and DoD can be made and scenarios with direct path and indirect path can be differentiated. When the DoA is equal to DoD, only the direct path is involved and on the other hand, when the DoA is not equal to DoD, there exists an indirect path. However, the measure of DoD is ambiguous because of the 2λ spacing between the 2 Tx.

3.4. Geometry

The geometry model followed for the presented height classification algorithm is shown in the Figure 3.9. The vehicle is assumed to be moving in the X-direction with a constant velocity v which is the same as ego-velocity v_{ego}. The velocity of the vehicle is called the ego-velocity. From the Figure, it can be seen that the position of the car is taken at the origin and the position of the target of height, h_t is defined by the x,y,z coordinates, along with the azimuth and elevation angle represented as θ and φ respectively. The radial distance to the target from the vehicle is represented as R_d.

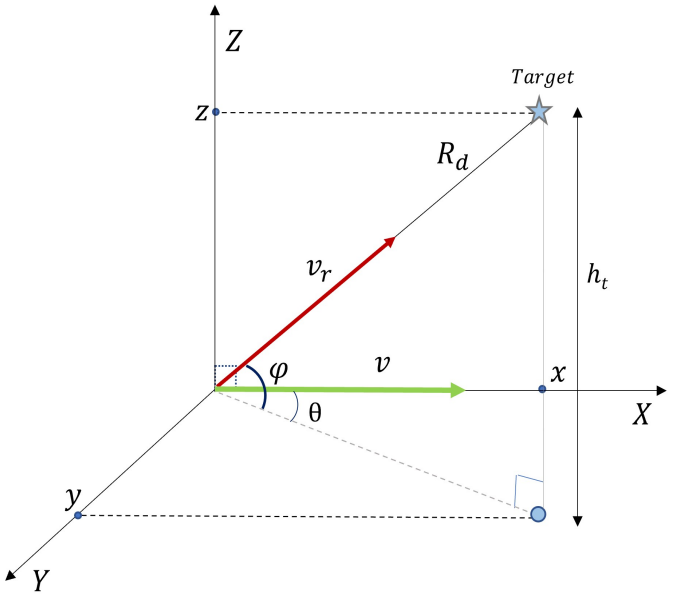

Figure 3.6: Geometry Model

Using geometry, the radial distance (R_d), azimuth (θ) and elevation angle (φ) with respect to the target coordinates can be formulated as follows:

$$R_d = \sqrt{x^2 + y^2 + z^2} \tag{3.16}$$

$$\theta = \text{atan}\left(\frac{y}{x}\right) \tag{3.17}$$

$$\varphi = \text{atan}\left(\frac{z}{\sqrt{x^2 + y^2}}\right) \tag{3.18}$$

These equations will be further considered in the Kalman filter section while defining the equations.

Assuming the vehicle moving towards a stationary target with an ego-velocity v_{ego} the radar mounted at the front of the vehicle will measure a radial velocity estimate v_r of the observed target. Since the target is stationary, v_r is the perceived velocity of the target, but in practice it is the velocity of the car. This radial velocity estimate under the influence of both azimuth and elevation angle information, can be formulated as:

$$v_r = v_{ego}.\cos(\theta).\cos(\varphi) \tag{3.19}$$

where θ is the azimuth angle and φ is the elevation angle of the target.

3.5. Flowchart of the proposed algorithm

The goal of this thesis is to achieve the 3-D classification of stationary targets. Due to the limited elevation estimation capabilities, the height information cannot be directly obtained. The core of the proposed algorithm revolves around the estimation of the elevation angle with the knowledge of the the ego-velocity. The ego-velocity estimation can be done using histogram techniques, and with the use of the Kalman Filter, the ego-velocity can be improved resulting in a more reliable elevation angle estimation.

In this section, the flow of information involved in achieving the aforementioned goal is discussed using the flowchart shown below. For every frame of measurements, a radar data cube is formed. Upon reception of the radar data cube for the respective frame, range-Doppler processing is carried out to estimate the range and velocity of the reflected targets. After identifying (detecting) the range and velocity bins of the targets, the snapshots are extracted to carry out DoA estimation using MIMO-Monopulse technique. At the next stage, an initial target list comprising of range, velocity and angle can be formed. Using the radial velocities and the angle parameters of the target, a velocity profile is created, which provides the means by which an initial ego-velocity estimate can be selected.

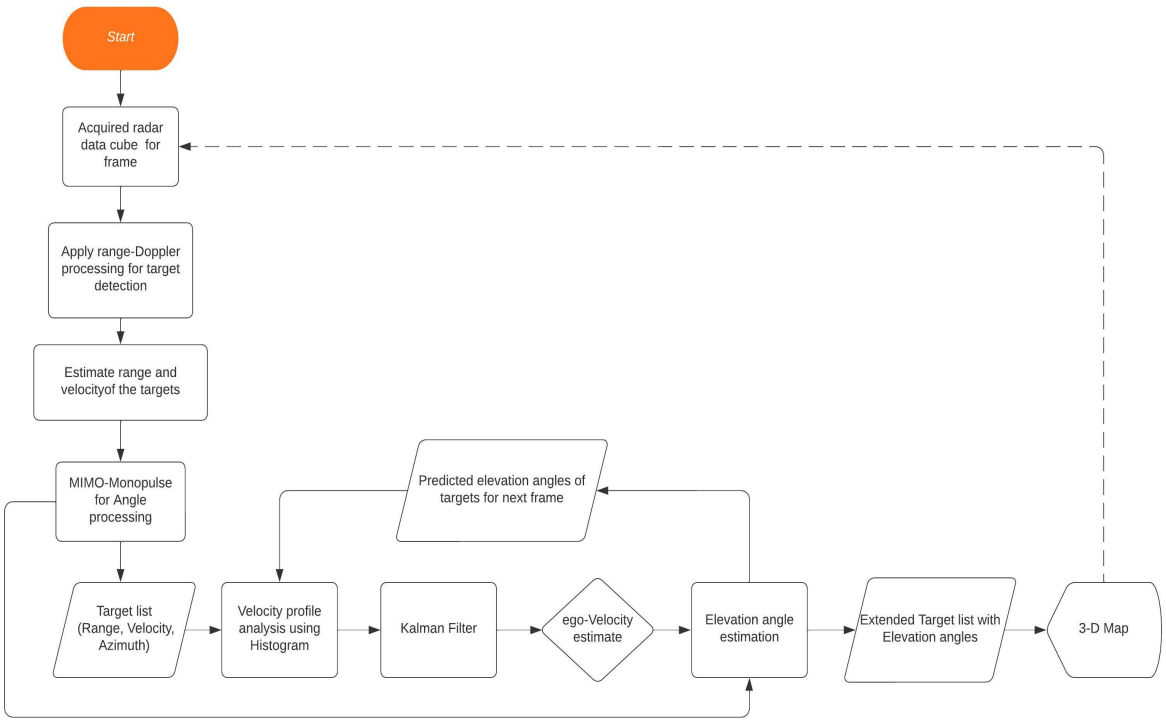

Figure 3.7: Flowchart representing depicting the flow of information using the presented approach

The distribution of the velocity profile in the form of a histogram is analyzed and an initial estimate of the ego-velocity is extracted. Furthermore, the extracted ego-velocity estimate is served as an input to the Kalman filter. The Kalman filter is designed to track the ego-velocity of the vehicle, thereby produces an ego-velocity estimate as an output as well as provides a prediction of the states of the stationary target as well. The improved ego-velocity parameter can then be used to estimate the elevation angles of the targets through pre-defined geometry and can also serve as an additional parameter in improving the histogram distribution for the next frame. After estimating the elevation angles of the targets, an extended target list can be created which is then passed on to create a 3-Dimensional map for the user. The process is then repeated for each frame and through multiple frames, the process delivers an improved estimate of ego-velocity, which in turn provides an improved estimation of elevation angles of the targets.

3.6. Ego-velocity estimation using velocity histogram

The idea behind the approach is to determine an initial ego-motion estimate from the reflected targets in the field of view (FoV). In this approach, the targets are assumed to be stationary. The distribution of radial velocity estimates from multiple targets is analyzed every measurement cycle to determine an ego-motion estimate which serves as an input to the Kalman Filter. This is done by creating a histogram, which is the approximation of the distribution for all the radial velocity estimates over the respective azimuth positions of the targets in a single frame. Using the histogram, the center of the highest bin (most occurring velocity) is assumed to be the best estimate of the ego-velocity with respect to the particular frame. Whether the right velocity bin can be sufficiently discriminated from other velocity bins depend on the number of bins, the bin width and the number of detections per frame. If the amount of bins are increased, then the amount of possible ego-motion estimates increases as well as the computation time. Hence, the increase in resolution along the X axis i.e. the velocity bin axis adversely affects the resolution on Y axis i.e. the number of values per bin, as multiple highest bins of the same size can occur and the wanted discrimination of ego-velocity compared to other velocities will deteriorate. In such situations, an appropriate value of the number of bins, is chosen. In spite, if multiple highest bins occur, the average of the center values of such bins can be taken as the best ego-motion estimate. Figure 3.8 provides a demonstration on how the varying binWidth affects the histogram bins, which in turn can affect the ego-motion estimate. The binWidth values seen below is taken in reference to the velocity resolution of 0.0089 km/h.

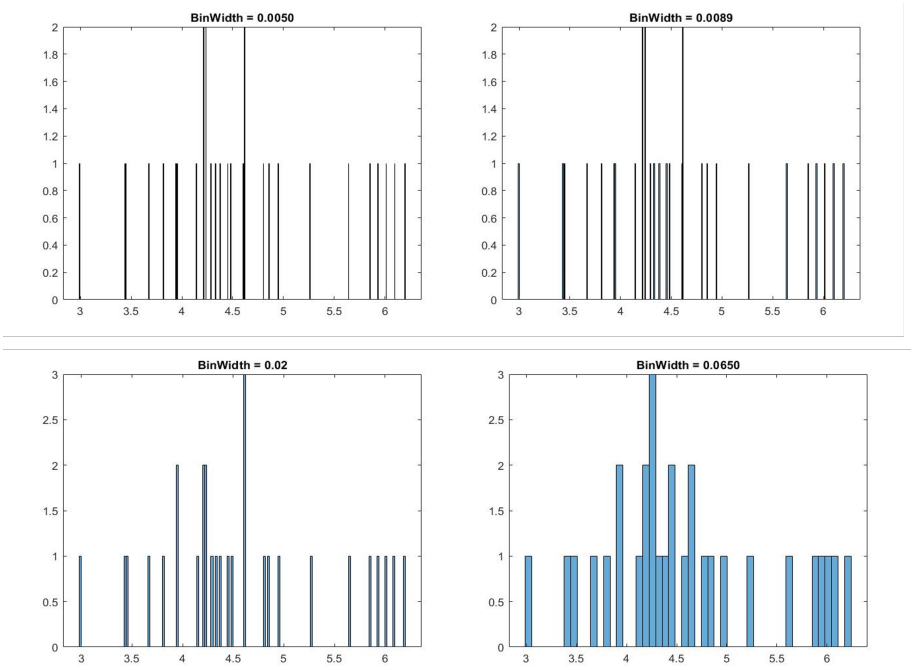

Figure 3.8: Effects of varying binWidth (km/h) in histogram distribution: X Axis represents the velocity values (km/h) and Y Axis represents the number of bins

For the first frame, since our antenna configuration does not produce an elevation angle measurement, the ego-motion estimate from the histogram will be biased. The Equation 3.19 points out the relation between ego-motion estimate and elevation angle. As a result, better the ego-motion estimate, better would be the elevation angle. Over the number of frames, the addition of elevation angles estimated using the Equation 3.19 can be fed into the histogram analysis, thereby gradually removing the bias. The idea is to have an improved estimate of the ego-velocity after a few measurement cycles through the use of an EKF with the help of elevation angle estimations. These elevation angle estimations will further improve the histogram distribution over the number of frames and produce an unbiased ego-motion estimate.

3.7. Target tracking using Kalman Filter

To improve the accuracy of the ego-velocity estimate, a Kalman filter is employed. The main idea behind the Kalman filter is to track the 2-D states of the targets and the ego-velocity in the Cartesian coordinates. However, the radar measurements in range, radial velocity and azimuth angle results in a non-linear function, due to which a 2-D Extended Kalman Filter is employed. To carry forward the working of the EKF, the radar measurements have to be converted to X-Y coordinates which involves non-linear conversion which is explained in Section 3.7.1. The ego-velocity estimate produced from the histogram is fed as an input to the 2-D Extended Kalman Filter, under the assumption of flat earth, i.e. no elevation angle. The states of the system for K targets are defined as follows:

$$X = R_{d,k}.\cos(\theta_k)\,; Y = R_{d,k}.\sin(\theta_k)\,; \dot{X} = -v_{ego}; \dot{Y} = 0 \tag{3.20}$$

where, k = 1,..,K.

The summary of the algorithm employed is shown in the table below. In the procedure, as our current antenna

Algorithm 1 Extended Kalman Filter in ego-Velocity estimation

Input: R_d, θ, v_{ego} **Output**: v_{ego}, φ

procedure EKF(v_{ego})
  if $p = 1$ **then** ▷ p - Frame number
    Initialize $\varphi_{1,K}$ = 0
    Extract the v_{ego} estimate from the histogram: $v_{ego,p} = histfunc(v_{r,k}, \cos(\theta_k), \cos(\varphi_{1,K}))$
  else
    Extract the v_{ego} estimate from the histogram: $v_{ego,p} = histfunc(v_{r,k}, \cos(\theta_k), \cos(\varphi_{\text{KF,p,k}}))$
    Estimate elevation angles: $\varphi_{p,k} = \cos^{-1}(v_{r,k}/(v_{ego,p}.\cos(\theta_k)))$
  end
  Estimate states of the system, $\boldsymbol{E}(S_p)$ ▷ Equation 3.21
  Obtain radar measurement data of the targets, $\boldsymbol{E}(Z_{p,k})$ ▷ Equation 3.22
  Compute Jacobian matrix, $\boldsymbol{H}_j$ ▷ Mapping radar measurements
  Compute Kalman gain, $\boldsymbol{K}_p$ ▷ Equation 3.36
  Update system states, $\boldsymbol{E}(S_{p,k})$ ▷ Equation 3.37
  Predict system states,$\boldsymbol{E}(S_{p+1,k})$ ▷ Equation 3.38
  Estimate elevation angle: $\varphi_{\text{KF,p+1,k}}$ ▷ Utilized in Step 6 for the next frame
  Compute average of the ego-velocity estimates over K targets ▷ Final ego-velocity estimate

configuration does not provide an elevation angle estimate, for the first frame, they are initialised to zero. Hence, in the velocity histogram analysis, the ego-motion estimate for the first frame will be biased. But moving on, from the next frame onwards, the histogram takes into account the elevation angle variables which provides a better initial ego-motion estimate. After extracting the ego-velocity from the histogram, the states of the system (target) per frame p, given by $\boldsymbol{E}(S_{p,k})$ can be expressed as:

$$\boldsymbol{E}(S_{p,k}) = [x_k \;\; \dot{x} \;\; y_k \;\; \dot{y}] \tag{3.21}$$

The radar measurement data, given by $\boldsymbol{E}(Z_p)$ can be expressed as:

$$\boldsymbol{E}(Z_{p,k}) = [R_{d,k} \;\; v_{r,k} \;\; \theta_k] \tag{3.22}$$

3.7.1. Coordinate Conversion function

Since the tracking is done in Cartesian coordinates, the state variables will be derived from the radar measurements, which are done in 2-D polar coordinates. Meanwhile from the above equations, there is a visible difference in the coordinate system of the state variables, which is in Cartesian and the radar measurements, which is in Polar. As mentioned in Section 2.7, following the Equation 3.37, the measurement update i.e. the measure of deviation of the predicted states from the given measurement, cannot be computed directly due to unobservable system states. Hence, a measurement conversion function or Coordinate conversion function is required, which is expressed as:

$$\boldsymbol{M}\left(S_p\right) = \begin{bmatrix} R_d \\ \theta \\ v_r \end{bmatrix} = \begin{bmatrix} f(x,y) \\ g(x,y) \\ h(\dot{x},\dot{y}) \end{bmatrix} \tag{3.23}$$

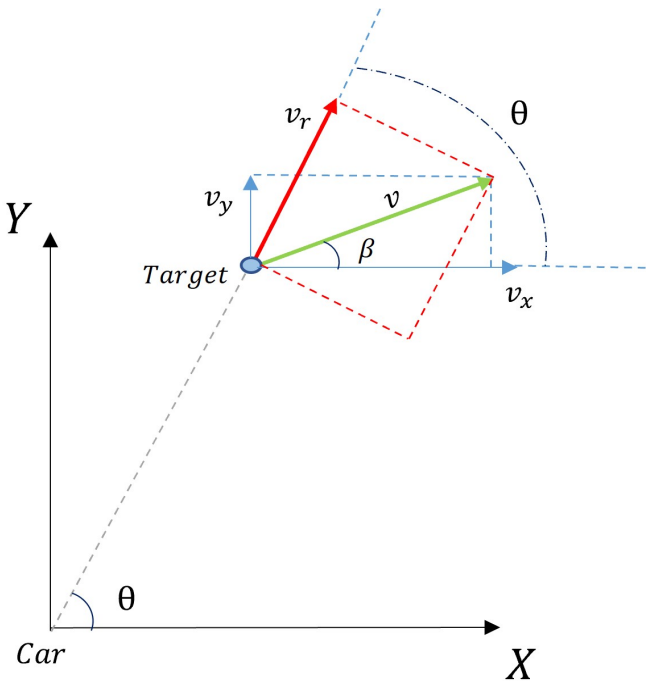

Figure 3.9: Expanding the X-Y axes in Figure

The geometry represents in general, the velocity components with respect to the target at an angle θ for a particular time instant. Considering at one point in the target trajectory, the tangential ego-motion vector v, creates an angle β, which can be expressed as:

$$\beta = \text{atan}\left(\frac{\dot{y}}{\dot{x}}\right) \tag{3.24}$$

From the Figure 3.9, incorporating the β, the v can be formulated as:

$$v_r = v \cdot \cos(\theta - \beta) \tag{3.25}$$

Substituting Equation 3.16, Equation 3.17 and v_r in $\boldsymbol{M}(S_p)$, we get:

$$\boldsymbol{M}\left(S_p\right) = \begin{bmatrix} f(x,y) \\ g(x,y) \\ h(\dot{x},\dot{y}) \end{bmatrix} = \begin{bmatrix} \sqrt{x^2+y^2} \\ \text{atan}\,2\,(y,x) \\ \sqrt{\dot{x}^2+\dot{y}^2} \times \cos\left(\text{atan}\,2\,(y,x) - \text{atan2}\,(\dot{y},\dot{x})\right) \end{bmatrix} \tag{3.26}$$

where, the notations of f, g, and h correspond to the radial distance (R_d), azimuth (θ) and radial velocity (v_{rad}) respectively. It is to be noted that these conversion functions hold for every target k, and every frame.

As mentioned in the Section 2.7, the Jacobian matrix $\boldsymbol{H}_j$ has to be computed for mapping the radar measurements between Polar coordinates and Cartesian coordinates and to linearly approximate the non-linear functions. The derivation and equations, in general, involved in the EKF are shown in Appendix B, for a single target i.e. k = 1, starting with the definition of $\boldsymbol{H}_j$ given as:

$$\boldsymbol{H}_j = \begin{bmatrix} \frac{df}{dx} & \frac{df}{d\dot{x}} & \frac{df}{dy} & \frac{df}{d\dot{y}} \\ \frac{dg}{dx} & \frac{dg}{d\dot{x}} & \frac{dg}{dy} & \frac{dg}{d\dot{y}} \\ \frac{dh}{dx} & \frac{dh}{d\dot{x}} & \frac{dh}{dy} & \frac{dh}{d\dot{y}} \end{bmatrix} \tag{3.27}$$

The matrix elements are calculated as follows:

$$\frac{df}{dx} = \frac{x}{\sqrt{x^2+y^2}} \tag{3.28}$$

$$\frac{dg}{dx} = \frac{-y}{x^2+y^2} \tag{3.29}$$

$$\frac{dh}{dx} = v \cdot -\sin(\theta-\beta) \cdot \frac{dg}{dx} \tag{3.30}$$

Similarly with respect to y,

$$\frac{df}{dy} = \frac{y}{\sqrt{x^2+y^2}} \tag{3.31}$$

$$\frac{dg}{dy} = \frac{x}{x^2+y^2} \tag{3.32}$$

$$\frac{dh}{dy} = v \cdot -\sin(\theta-\beta) \cdot \frac{dg}{dy} \tag{3.33}$$

$$\frac{dh}{d\dot{x}} = \frac{\dot{x}\cos(\theta-\beta) - \dot{y}\sin(\theta-\beta)}{v} \tag{3.34}$$

Similarly,

$$\frac{dh}{d\dot{y}} = \frac{\dot{y}\cos(\theta-\beta) + \dot{x}\sin(\theta-\beta)}{v} \tag{3.35}$$

In this manner, $\boldsymbol{M}(S_p)$ is approximated using the Jacobian matrix $\boldsymbol{H}_j$ in equations to maintain linear transformations. These derived general equations are adapted to the states of the system defined in Equation 3.20.

The Kalman gain is computed as follows:

$$\boldsymbol{K}_p = \boldsymbol{P}_{p,p-1}\boldsymbol{H}_j^T \left(\boldsymbol{H}_j \boldsymbol{P}_{p,p-1}\boldsymbol{H}_j^T + \boldsymbol{R}_p\right)^{-1} \tag{3.36}$$

where, the covariance parameter, $\boldsymbol{P}$ can be updated and predicted for the frames respectively using the Equations 2.22 and 2.19.
The state of the system is updated using the Equation given below:

$$\boldsymbol{E}(S_{p,k}) = \boldsymbol{E}(S_{p-1,k}) + \boldsymbol{K}_p.(\boldsymbol{E}(Z_{p,k}) - \boldsymbol{H}_j.\boldsymbol{E}(S_{p-1,k})) \tag{3.37}$$

Furthermore, using the state transition matrix $\boldsymbol{F}$ of a 2-D constant velocity model with respect to the defined system states, the states of the system for the next frame is predicted which can be expressed as:

$$\boldsymbol{E}(S_{p+1,k}) = \boldsymbol{F}.\boldsymbol{E}(S_{p,k}) \tag{3.38}$$

where,

$$\boldsymbol{F} = \begin{bmatrix} 1 & \Delta t & 0 & 0 \\ 0 & 1 & 0 & 0 \\ 0 & 0 & 1 & 0 \\ 0 & 0 & 0 & 0 \end{bmatrix} \tag{3.39}$$

$$\tag{3.40}$$

Using the updated and predicted value, the R_d, θ and φ can be updated and in particular the updated φ estimates can be fed back into the histogram phase. This is done in order to have a refined estimate of ego-velocity estimate from the histogram. Utilizing this process over the frames, i.e. as the vehicle moves towards a target, the ego-motion estimate is improved, thereby providing a better estimate of the elevation angle of the target.

3.7.2. Conclusion

In this chapter, the flow of information along the signal processing chain is discussed to provide a clarity in the working of the proposed algorithm. First, the application specifications considered in the thesis are presented, providing the antenna configuration which is employed and the significant requirement of a low latency DoA estimation technique based on a single snapshot. To enable the latter requirement, the monopulse technique is explained, followed by its application in MIMO radar i.e. MIMO-Monopulse. The working of ACM and PCM are discussed in detail. The ACM is employed in the DoA estimation phase in the proposed algorithm. The basic approach of the ACM is that the received signals are used to generate sum and difference beams through digital beamforming (DBF), which can be used to compute a monopulse ratio in order to produce a precise DoA estimation. As an additional feature to create a distinction in direct path and indirect path, a simple application of phase comparison monopulse was also employed which can help in estimating the DoD in a NLOS scenario. Subsequently, before moving into the target tracking using Kalman filter, the geometry model defined for the proposed algorithm is presented, using which the equations for radial distance, azimuth and elevation of the targets are derived. The ego-motion estimation holds a significant value in the estimation of elevation angle. Using the geometry model, a 2-D Extended Kalman Filter was designed as a means to track the ego-velocity and the steps involved in performing the algorithm are summarized in Table 1. The working of the 2-D EKF, along with the state space model is explained in detail using equations. Furthermore, a histogram approach was used in the velocity profile analysis, to provide a refined input of the ego-velocity estimate per frame to the Kalman filter. As we go through the flow of information, it is shown that the elevation angle estimated per frame at the end of the Kalman filter operation, is used in improving the histogram for the successive frame, thereby providing an improved unbiased ego-velocity estimate. Through multiple iterations or frames, these ego-velocity estimates can be used to estimate the elevation angles of the target, thereby providing a fast and precise 3-Dimensional height classification algorithm.

4

Simulation Results

In this chapter, the simulation analysis of the proposed height classification algorithm is presented using the MATLAB software. Improvements made using the presented approach, has been supported with results through Monte-Carlo simulations and the performance parameters are studied. The goal of carrying forward these simulations is to determine the improvement in ego-velocity using the histogram approach presented. The improvements made using the presented approach has been supported with results through Monte-Carlo simulations and the performance parameters are studied.

For the simulations, the targets are present at various orientations and the car is moving towards the targets as depicted in the geometry shown in Figure 3.9. The radar specifications applied are summarised in the table below:

Number of transmit antennas	3
Number of receive antennas	4
Bandwidth	1 GHz
Number of pulses	256
Sample Frequency	20 MHz
PRI	25.6μs

Table 4.1: Radar Specifications

MIMO array using 3 Tx's and 4 Rx's with an inter-antenna spacing of $\lambda/2$ i.e. a ULA is employed. Utilizing these specifications, the measurement parameters with respect to range and velocity can be computed, which is given by:

$$R_{max} = 19.2m \quad | \quad \Delta R = 0.15m \quad | \quad \Delta V = 0.0089km/h \quad | \quad V_{max} = 5km/h$$

To initialize the simulations, 30 stationary targets are created in the x-y-z plane and a trajectory directing towards the automobile i.e. assuming the motion of the automobile along the x-axis, is created to emulate the real-time tracking with a SNR of 20dB. The target are distributed within 10 to 18m in the x axis, -5 to 5m in the y axis and 0 to 4m in the z axis. The visualization of the targets i.e the direct path of the radar reflections can be seen in the Figure below.

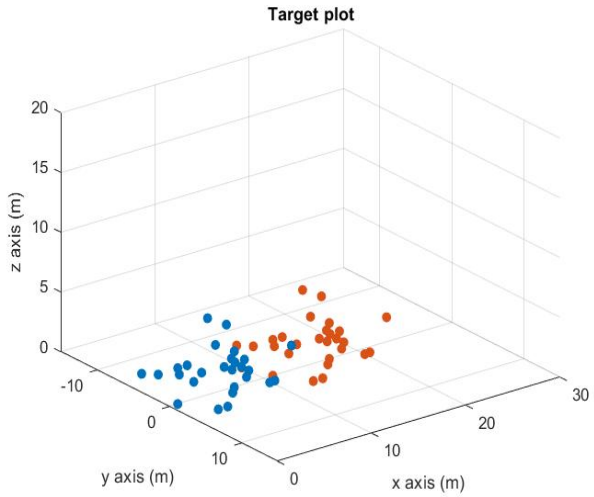

Figure 4.1: Isometric view on the position of the targets and the color shift represents the motion of the vehicle towards the targets. The orange color represents the initial position of the targets and the blue color represents the positions at the end of the measurement

4.1. Simulation process

Before proceeding with the simulation of the proposed algorithm, using the aforementioned target distribution within the x-y-z axes, 1000 stationary targets were created. This is done to provide a validation to the histogram approach. Since the target is stationary, v_r is the perceived velocity of the target, but in practice it is the velocity of the car i.e. ego-velocity. From the Figure 4.2b, the histogram shows that one can expect the ego-velocity being the most occurring velocity which supports the idea of the highest bin in the histogram giving the best ego-velocity estimate. In principle, higher velocities than the ego-velocity cannot occur, unless they come from the moving targets. Furthermore, due to noise, one can expect certain detected velocities larger than ego-velocity.

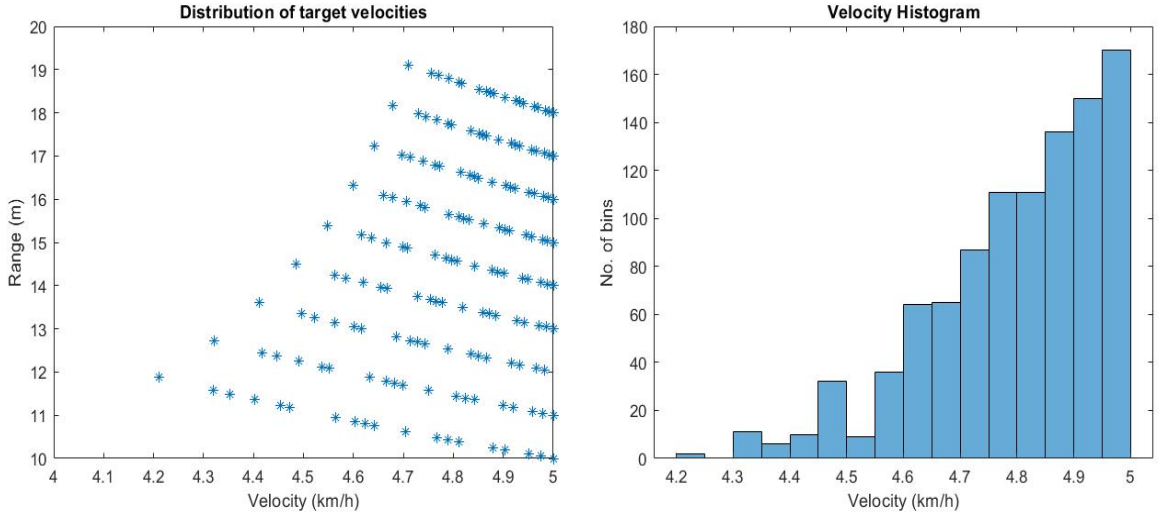

(a) X-Y plot representing the distribution of radial velocities

(b) Histogram representation of radial velocities

Figure 4.2: Validation of velocity histogram

Following the flowchart discussed in Figure 3.7, on acquiring the radar data cube consisting of target information with respect to the initial simulation parameters of 30 targets, range-Doppler processing as shown below in Figure 4.3b is carried out to determine the range and velocity bin of the targets for the subsequent DoA processing using MIMO-Monopulse.

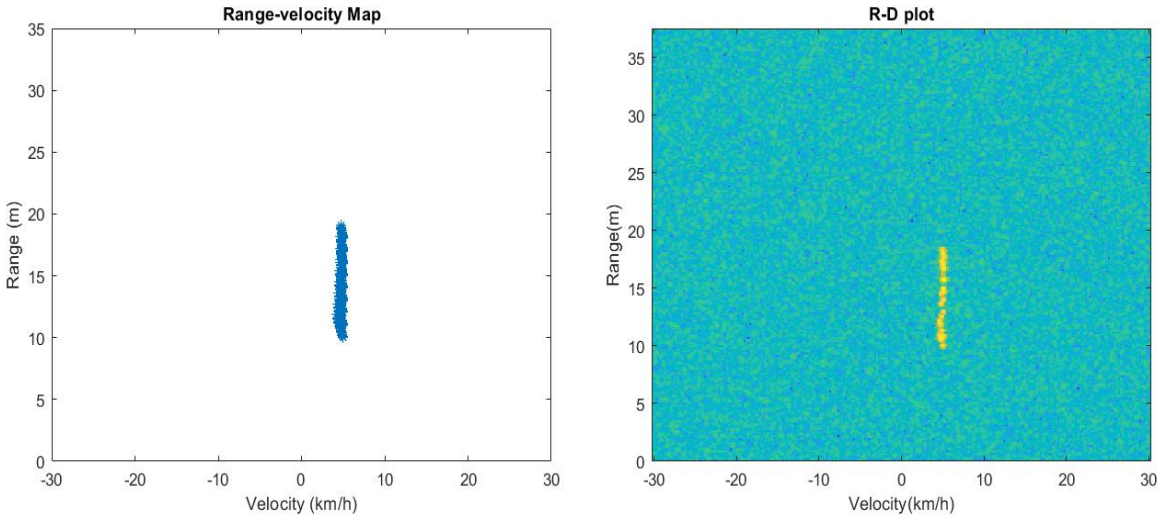

(a) X-Y plot representing the distribution of 1000 targets

(b) The range-Doppler map of the detected 30 targets

Figure 4.3: Representation of the target information

The deviation of the detections or the bending of the line observed in the Figure 4.3b is due to the influence of elevation and azimuth angles on the radial velocity and distance of the targets. Comparing the plots in Figure 4.3, the bent line in the range-Doppler map could be thought of as the realization of 30 random targets. After the range-Doppler and angle processing, a target list is created comprising the range, velocity and angle parameters. Using the target list generated along the trajectory of the vehicle, the algorithm using the histogram approach was simulated for an initial ego-velocity of 5km/h.

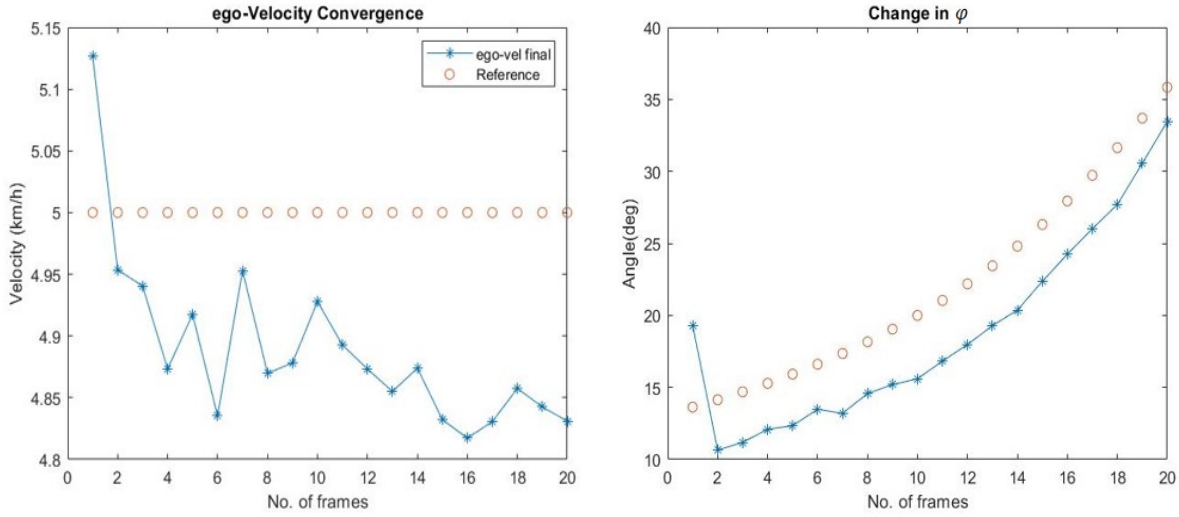

(a) ego-Velocity estimates

(b) Elevation angle estimates

Figure 4.4: (a) Convergence of ego-motion estimates over multiple frames. (b) Evolution of elevation angle estimates for a particular target over multiple frames. **Note:** The red circles represent ground true elevation of the target

Observing the convergence plot in Figure 4.4a, we can see that the ego-velocity estimates do not converge to the reference value of 5km/h. This is due to the limitations of the application of 2-Dimensional KF as the elevation angle is not tracked in particular or defined in the states of the system. However, the algorithm is able to estimate the ego-velocity with an average error of 0.15km/h. The effect of the ego-velocity can be seen in the elevation angle estimates as it improves over the frames. The elevation angle estimates can then be used to estimate the height in the z-coordinate. To illustrate the procedure, looking at the Figure 4.5 the target plot is shown with the estimated position of 30 targets in a particular frame computed using the proposed algorithm. The elevation angle

estimates produced are used to estimate the height in the z-coordinate as shown in the Figure 4.6a, which then can be used in the height classification to deem it as traversable, non-traversable or a pass through object.

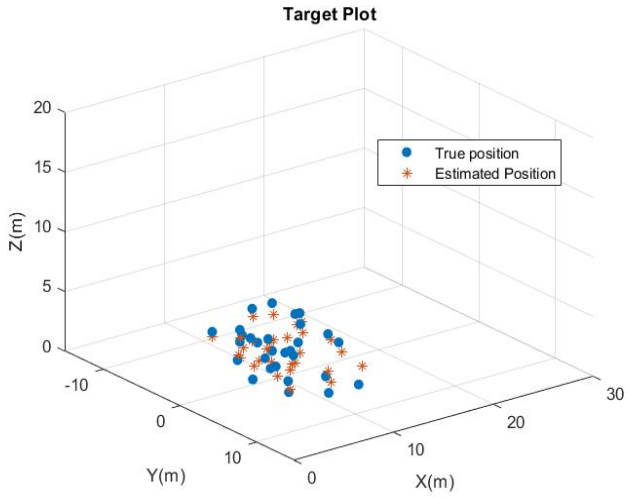

Figure 4.5: Target plot with true positions and estimated positions

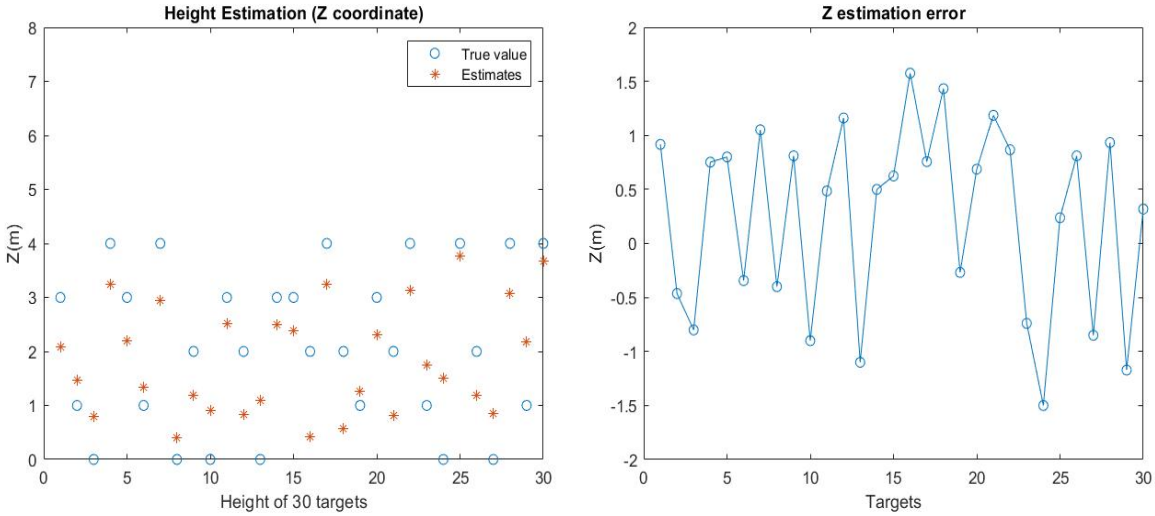

(a) Comparison of Z estimates of targets with true values

(b) Error in Z coordinate estimation of respective targets

Figure 4.6: Height estimation (Z-coordinate) of 30 targets of one random realization of 30 targets

The height estimation error is shown in Figure 4.6b which is related to the height of 30 targets of one random realization of 30 targets. Although we get an undesirable maximum error of +/- 1.5m, the concept is that over the number of frames, as the ego-velocity improves, better would be the elevation angle estimates. Thereby, reducing the Z coordinate estimation error or the height estimation error.

4.2. Comparison

In this section, the improvement offered using the application of velocity histogram in estimating the ego-velocity is shown in contrast to the application without histogram.

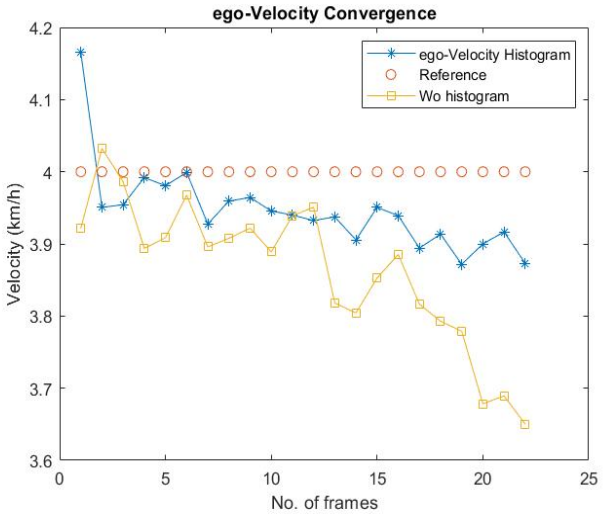

Figure 4.7: Showcasing the improvement using Histogram approach for a single iteration

In the Figure 4.7, the simulation was conducted for an ego-velocity of 4km/h over a single iteration consisting of 20 radar frames with a SNR of 20 dB. The purpose of histogram to diminish the errors due to the elevation angles and azimuth are evident in the improvement of ego-velocity using the histogram method.

To validate the consistency of the proposed algorithm, the performance of the algorithm was tested by performing Monte-Carlo simulations. The algorithm was run for 1000 iterations each consisting of 20 radar frames. The goal is to achieve a constant change in bias while using the velocity histogram in the proposed algorithm. The observations are plotted below:

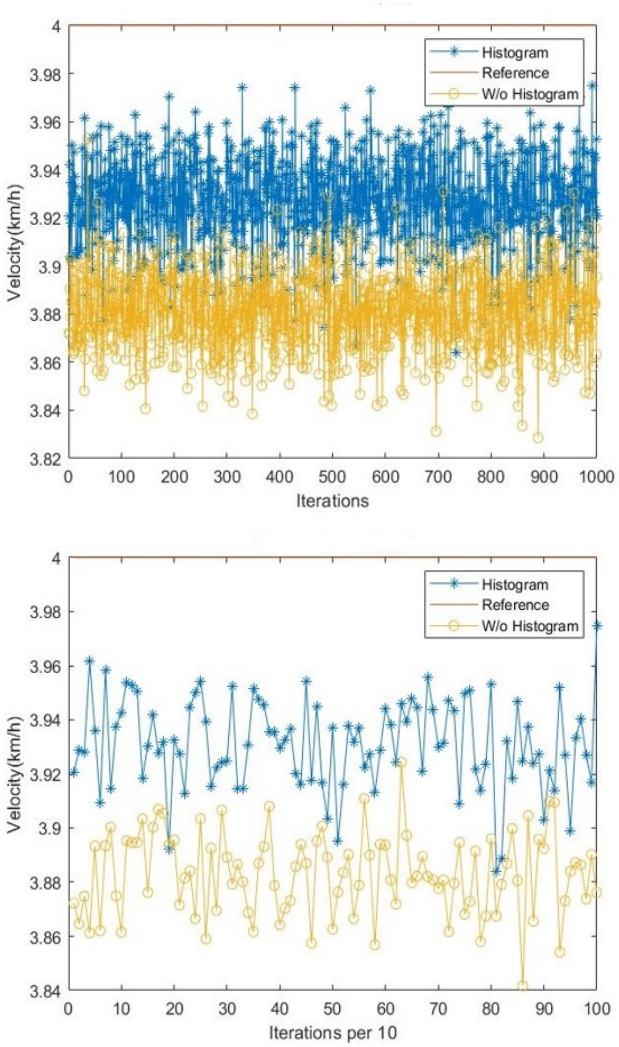

Figure 4.8: Monte Carlo Simulations of the algorithm using Histogram and without Histogram Approach: **Top** - Ego-motion estimates of 1000 iterations. **Bottom** - Exploded view of ego-motion estimates at every 100 iterations

The goal of carrying forward these simulations is to determine the consistency of improvement in the ego-velocity estimates using the velocity histogram approach. From the Figure 4.8, we can infer that there is a consistent and constant improvement in the ego-velocity estimates using the velocity histogram approach as opposed to the approach without using the histogram method. The following distinction between the approaches can be noted using the legend. The simulation was carried out for a reference ego-velocity of 4km/h.

Looking at the Figure 4.8, there is a visible bias with respect to both the approaches. However, the bias is smaller with the application of the velocity histogram. The bias comes from the limitations of the 2-Dimensional KF and the elevation angle is not being tracked in particular in the KF. Due to this reason, as previously mentioned, the true convergence is not achieved. On the contrary, in comparison with the non-histogram approach, the bias is larger as the errors in ego-velocity in every frame accumulates and there is no improvement in the estimation. It changes as a function of ego-velocity, also with the errors in the elevation angle and azimuth domain. We can attain an improvement in the range of 0.06-0.08 km/h using the proposed algorithm. Equation 3.19 highlights the importance of having an improvement in ego-velocity using the proposed algorithm in the estimation of elevation angles.

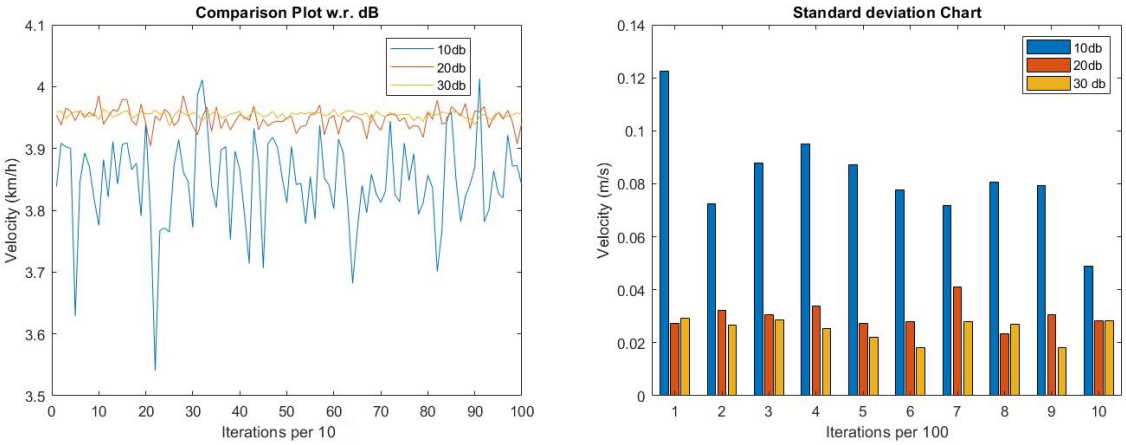

(a) ego-Velocity estimates **(b)** Standard deviation plot

Figure 4.9: Monte-Carlo Simulations of the proposed algorithm with the velocity histogram for varying SNR

The simulations were carried out for varying SNR (Signal-to-Noise Ratio) to determine the variation in ego-velocity estimates and subsequently, the standard deviation chart is also plotted to determine the extend of deviation under the influence of low to high SNR. For SNR of 10dB, as expected from the Figure 4.9, a deviation of 0.06 to 0.12 m/s (0.2 to 0.4km/h) can be seen. A much less deviation of 0.02 to 0.04 m/s (0.07 to 0.1km/h) as well can be seen for 20dB and 30dB SNR.

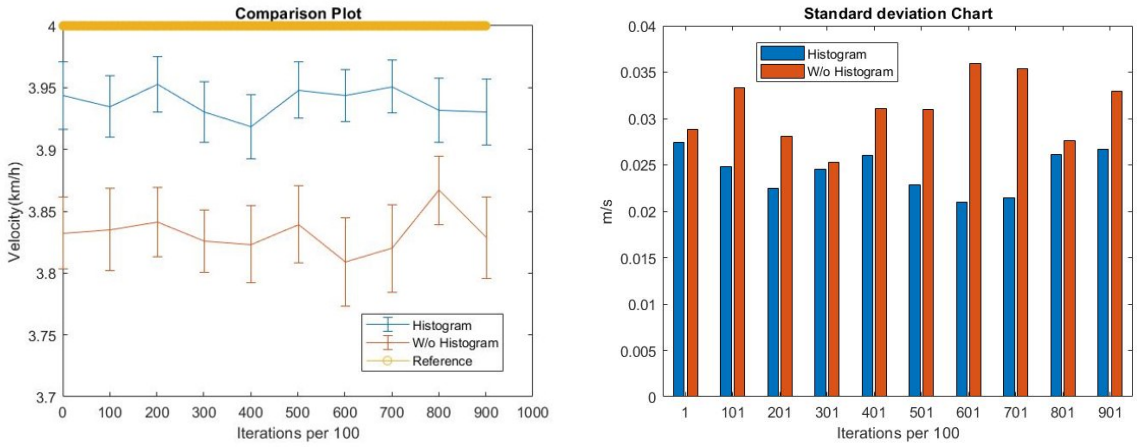

(a) ego-Velocity estimates **(b)** Standard deviation plot

Figure 4.10: Monte-Carlo Simulations using Histogram and without Histogram

To determine the standard deviation for two approaches one being the Histogram approach and the other being the one without Histogram approach was tested. From the Figure 4.10, it is represented in the form of error bar as well as a bar graph for a better understanding. Comparatively, more deviation is seen in the algorithm without applying the histogram method.

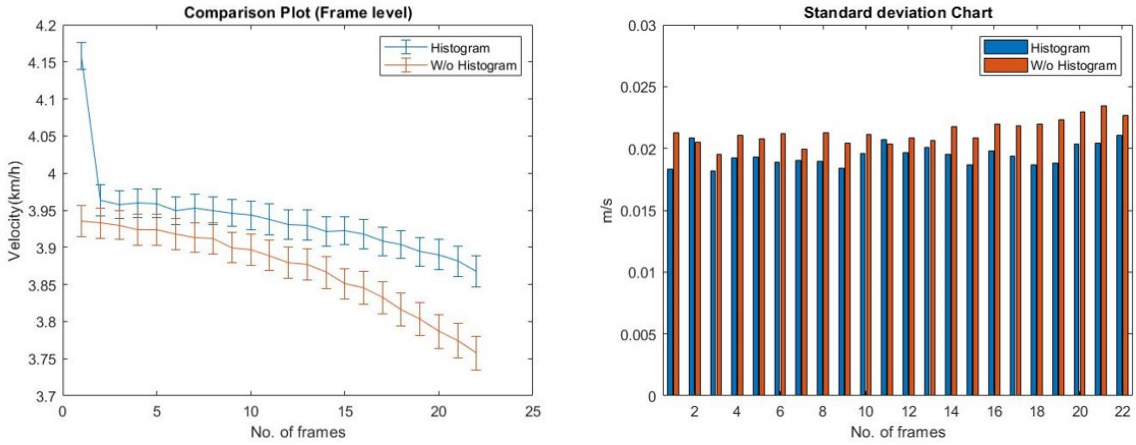

(a) ego-Velocity estimates

(b) Standard deviation plot

Figure 4.11: Monte-Carlo Simulations (Frame level)

Monte-Carlo simulations were carried out in the frame level, i.e. for every frame multiple iterations were carried out to understand the impact of the proposed algorithm in each and every individual frame. A standard deviation chart is plotted as well and we can infer that the ego-velocity estimates within a particular frame is improved using the histogram approach as opposed to the algorithm without the histogram approach.

The ego-velocity estimates will not completely converge to the reference velocity of 4 km/h due to the influence of the elevation angles and the assumptions of the proposed Kalman Filter model as discussed in Section 3.7. To improve the algorithm in further, and to track the elevation angles in particular as well, an extended 3-Dimensional KF can be used.

4.3. Conclusion

In this chapter, the simulation results of the proposed algorithm using MATLAB software was presented. Using the ego-velocity estimates, the elevation angles of the target was produced. Subsequently, the 3-Dimensional map was produced by estimating the height using the Z coordinates. The performance of the proposed algorithm is studied, tested and compared to the approach with the histogram and verified thorough Monte-Carlo simulations. Scenarios with different levels of SNR was used to analyze the performance of the algorithm and the comparison was made using the standard deviation parameter. Furthermore, the convergence plots of the algorithm in regard to the reference ego-motion and elevation angle of a particular target was also presented. In these simulations, it was apparent that the proposed algorithm using the histogram approach provided a consistent improvement in ego-motion as opposed to the one without the histogram. However, true convergence could not be achieved due to the application of the 2-Dimensional EKF but can be improved in the future using a 3-Dimensional EKF.

5

Experimental Validation

To validate the estimation results in the ego-motion and elevation angle of targets obtained from the simulation model in Chapter 4.1, measurements from real-time experiments in an outdoor environment carried out by N. Petrov in his project, was used which was provided through internal communications [46]. The experiments were carried forward using the Fully-Integrated 77 GHz Radar Transceiver, provided by NXP Semiconductors, mounted on the front of the automobile. The goal is to utilize the real measurement data consisting of the target parameters such as range, velocity, and angle (azimuth) in testing the proposed algorithm in creating a 3-Dimensional map using the estimated ego-Velocity and elevation angles.

5.1. Measurement Setup

The real-measurement was conducted in the premises of TU-Delft, using an automobile with the radar mounted in the front of the vehicle as shown in the Figure 5.1. The radar specifications are summarized in the Table below:

Number of transmit antennas	3
Number of receive antennas	4
Bandwidth	1 GHz
Carrier Frequency	78 GHz
Number of Chirps	256
Sample Frequency	20 MHz
Number of FPS	10

Table 5.1: Radar Specifications

Figure 5.1: Measurement Setup

For visual reference, the camera is placed on the deck which can be used to align the 3-Dimensional estimates of the target using the proposed algorithm. The real-time image also provides the velocity of the automobile through GPS which shall be useful in validating the ego-motion estimate produced using the proposed algorithm in the following sections below.

Figure 5.2: Visual reference

5.2. Observations

This section provides an overview of the results obtained through the various phases of the processing of the real measurement data. The real measurement data received consisted of a detection list comprising of the range, angle (θ) and velocity of the respective target. The Figure 5.3 depicts the comparison of the 2-Dimensional estimates directly from the radar with the 2-Dimensional estimates from the proposed algorithm for the particular frame. The 2-D estimates were predicted for the particular frame using the proposed algorithm and similar detections were to be found with the radar measurement and almost accurate, for instance, the detection marked using a circle. The following processing is done to validate the algorithm in 2-Dimensions, before proceeding to 3-Dimensions. We can also observe a few missing detections as there was a limit on the detections considered for the algorithm due to the association factor, which is outside the scope of this thesis.

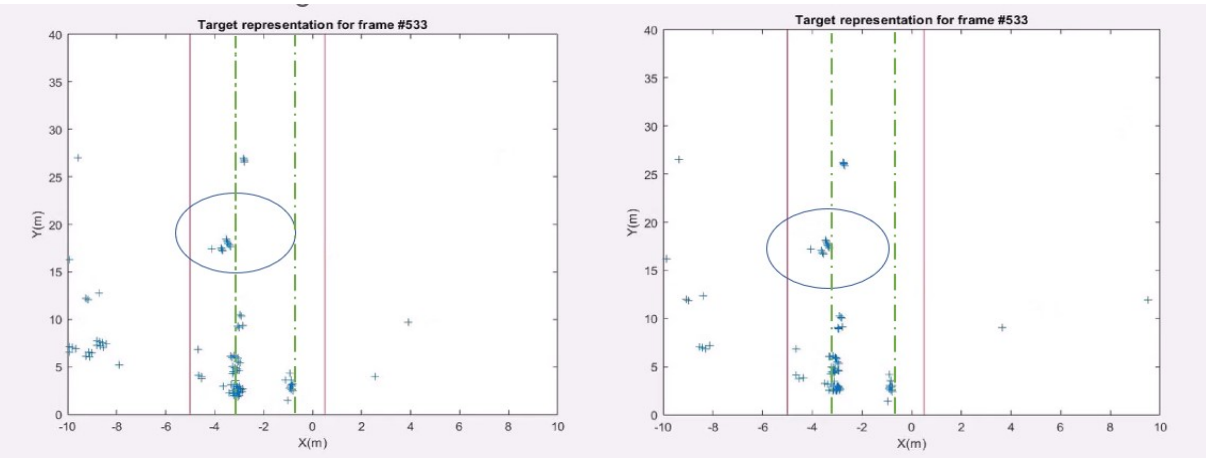

(a) 2-Dimensional estimates from radar

(b) 2-D estimates from proposed algorithm

Figure 5.3: Comparison plot displaying estimates in 2-Dimensions. The red vertical line represent the building boundary and the green dotted vertical line represents the outline of the street.

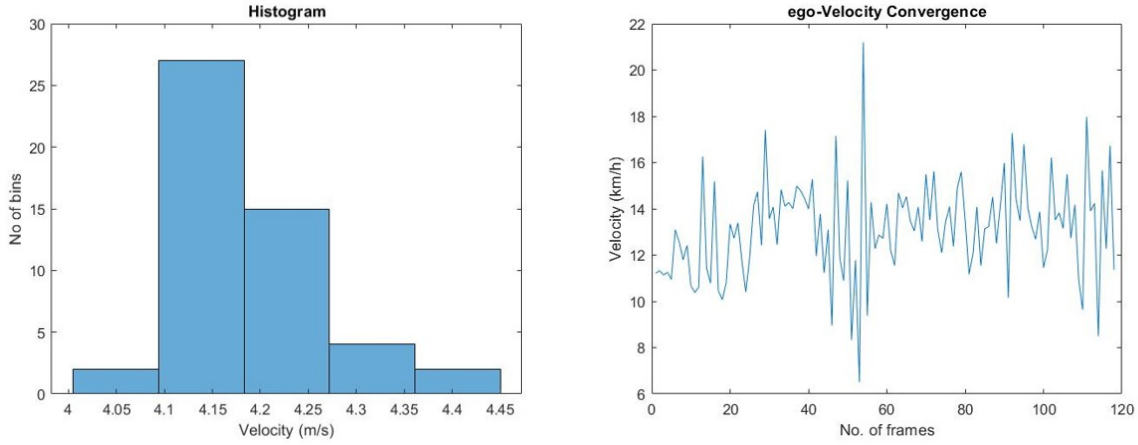

(a) Velocity histogram

(b) ego-Velocity estimations using the proposed algorithm

Figure 5.4: Real Measurement data 1: ego-Velocity estimation

From Figure 5.4, the ego-velocity estimation was performed and the velocity histogram can be seen. It can be observed that center of the highest bin provides us at 4.13m/s which can be equated to 14.8 km/h. The actual velocity of the car as recorded from the dash camera is around 15km/h (4.16m/s). By decreasing the process noise, the following ego-estimation curve can be smoothed out. However, from the velocity histogram in Figure 5.4a, we can see a number of bins with velocities higher than the ego-velocity. This is because in practical scenarios/reality, there exists moving targets and those velocities can thought to be as radial velocities. The noise factor and the manual increase in the speed of the vehicle can also lead to having certain detected velocities larger than the ego-velocity as highlighted in Section 4.1. In an attempt to validate the ego-motion tracking aspect of the algorithm further, a particular incident was used. In the particular frame shown below, there appears to be an unfortunate cycle crash and in reality, there is a reduction in velocity of the car due to the braking. The algorithm was run for the particular set of frames which covers the event and this particular reduction in velocity was noted, where the desired result would be to have them aligned with the ego-velocity estimates produced using the proposed algorithm. The comparison plot used for validation is shown below.

Figure 5.5: Real Measurement data 2: Validation of ego-velocity tracking

Using the proposed algorithm, the ego-velocity was estimated and tracked across the set of frames. The reference velocity of the car is found to be around 15km/h. As expected, the plot depicts a drastic reduction of ego-velocity i.e. from 15km/h to 8km/h approx due to the cycle incident which validates the ego-motion tracking aspect of the algorithm.

The next step is to produce a 3-Dimensional map using the elevation angle estimates that is computed from the ego-velocity estimates using the Equation 3.19. Association of targets is important during the processing of the real measurement data to produce a 3-Dimensional map. In reality, the procedure is done using the NXP module as part of the pre-processing. However, in this scenario/case, to simplify the processing, a rough manual association with respect to the Z coordinates was performed to determine if the detections belong to the same target. The following equations shown below are used to produce the 3-Dimensional map with respect to the X, Y and Z coordinates.

$$X = R_d * \cos(\theta) * \cos(\varphi) \tag{5.1}$$

$$Y = R_d * \sin(\theta) * \cos(\varphi) \tag{5.2}$$

$$Z = R_d * \sin(\varphi) \tag{5.3}$$

For the following real-measurement results shown below, around 50 detections from a single frame were taken, after which the manual association was conducted before proceeding to carry out the proposed algorithm. The 3-Dimensional map created from the estimates of the proposed algorithm, is compared with the targets in the camera image. The targets in focus are marked by oval shapes with respective colors to correlate with the video frame. Looking at the detections in plots, different color codes within the contour can be seen as it represents different elevation features. Visually, for reference purposes, the outline of the road has been marked with a width of 4m to align with the road seen in the camera image. To correlate the target detections in the plot with the video frame, standard measurements of the target was used i.e. the length of the street light pole of around 6-7m and the distance between the street lamps of around 18-19m was referred.

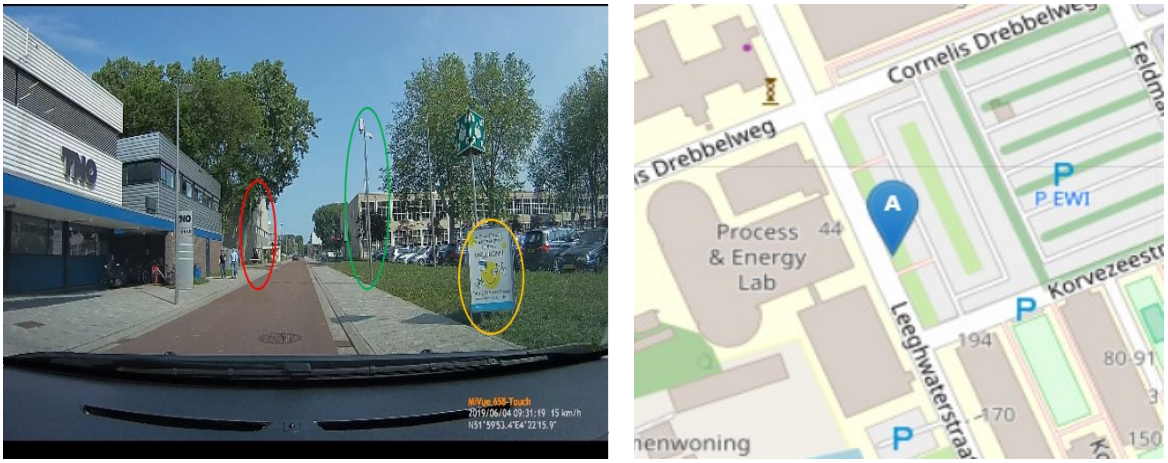

(a) Image from the camera for the particular frame

(b) Corresponding GPS coordinates for the frame

Figure 5.6: Real Measurement data 3

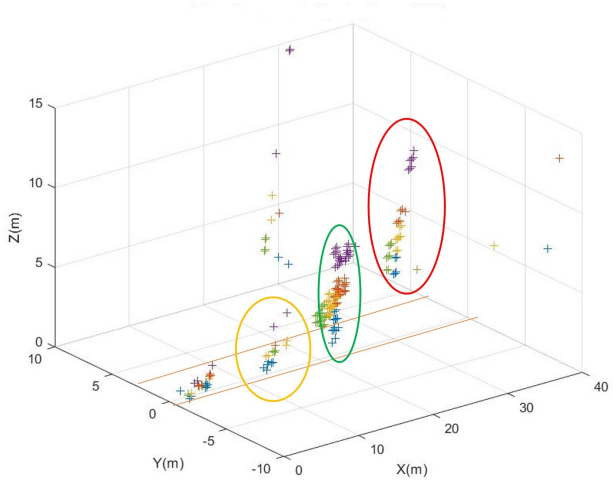

Figure 5.7: Real Measurement data 3: The red, yellow and green color is used to cluster the extended objects. The horizontal lines represent the outline of the street

The Figure 5.6 shows the video image of the frame showcasing the targets of interest. Utilizing the GPS coordinates of the respective frame, we can validate the location of the car which correlates to the video image. From the Figure 5.7, in comparison to the respective video image of the frame, the signal board, and two lamp posts were detected. The height estimation of lampost was found to be around 7m. The error in height estimations can be attributed to the error in ego-velocity. Due to the limit on the detections taken due to association factor, the cluster of detections belonging to the TNO building on the right hand side and the subsequent lamp post was not visible. However, we can see some detections on the right hand side within the Z coordinate estimate of 4-6m that comes from the reflections of the building.

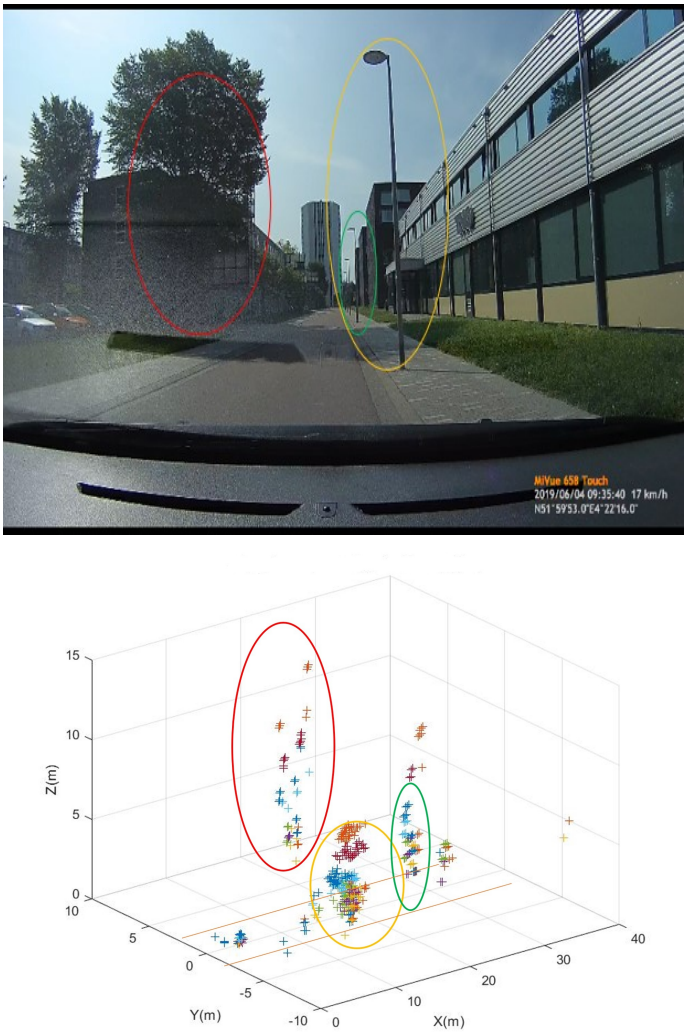

Figure 5.8: Real measurement Data 4: **Top** - Image from the camera for the particular frame. **Bottom** - The red, yellow and green color is used to cluster the extended objects. The red horizontal lines represent the outline of the road.

From the Figure 5.8, the detections seen in the 3-Dimensional map is produced from the elevation angle estimates using the proposed algorithm. On comparing the particular detections in the plot to the camera image, we can see three distinct targets, the lamp post, tree and the subsequent lamp post at around 20 - 30m range. We can also see some reflections from the ground at an early distance. Some reflections from the building entrance on the right can also be seen beside the green contour (lampost). However, due to the association factor which is not in the scope of this thesis, only 50 detections from a single frame were considered. From Figure 5.8 and Figure 5.7, we can see that at the initial distances, there appears to be a cluster of detections which can be attributed as ground reflections.

5.2.1. Conclusion

In this chapter, the results from the real-time experiments using the Fully-Integrated 77 GHz Radar Transceiver, provided by NXP Semiconductors, mounted on the front of the automobile, conducted in the outdoor premises of TU-Delft were presented. The proposed algorithm was able to provide a 3-Dimensional map of the surroundings detailing its height information along with the ego-motion estimation. The visual images from the camera was used as a reference to align the results from the proposed algorithm and was able to point out the detections to the respective object or targets in the image. An accurate tracking of the ego-motion was also achieved.

6

Conclusion

In this section, the work conducted on this thesis will be summarized with respect to the novelty and results obtained, using which certain conclusions will be drawn. This opens and sets up the platform to provide and implement further research ideas on this topic, which shall be discussed in Section 6.2. Furthermore, the challenges faced during the project and in the experimental validation phase will be touched upon along with a solution prospect in the future.

6.1. Results and Novelties

Radars hold a significant value in providing the safety factor in autonomous driving as they can be used for detection of road objects, pedestrians, cyclists and other vehicles. The important factor with respect to the targets is its height information which can help in classifying the targets, and give the necessary information to the driver to make a decision regarding whether to go over, under or through the object. The main challenge for automotive radar system of not having the height information (elevation measurements) in the object detection in the driving direction is addressed in this project. To carry out the height estimation procedure, ego-motion estimation plays a significant role. This work introduces a novel algorithm that jointly carries out ego-motion estimation and provides a 3-Dimensional map of the surroundings i.e. a low complexity and fast target height classification algorithm was developed to achieve the research goals mentioned in Section 1.3. The suggested approach utilizes a single snapshot of data obtained following range-Doppler processing, enabling simple integration and quick response times. The radar scene was assumed to be of stationary targets and the orientation of the radar covers the azimuth domain. To enable this quick response automotive radar system, DoA estimation technique using a single snapshot along with the approach of 2-Dimensional Extended Kalman Filter was used.

A MIMO radar system is employed with 3 Tx's and 4 Rx's with the inter-element spacing of $\lambda/2$, creating a ULA. In achieving a low compexity and fast target classification algorithm, low latency becomes a key requirement. In the DoA estimation aspect of the project, super resolution techniques like MUSIC, ESPRIT offers the disadvantages in estimating DoA using a single snapshot due to the factor of correlated signals in subspace calculation. As a result, MIMO-Monopulse technique was used to determine the target DoA's. Taking into account the cost effectiveness and ease in implementation, ACM was used to determine the DoA, while an approach using PCM was conducted as an extra feature in being able to distinct the multipaths from direct path using the DoA and DoD information.

The velocity of the automobile or the ego-velocity is important as it helps in determining the height of the objects through the height estimation technique of Doppler beam sharpening. In the current state of the ego-motion estimation, a velocity profile is created using the radial velocities of the targets and its respective azimuth positions and analyzed. However, employing this approach leads to a biased velocity estimator as the elevation angle is not incorporated. In this work, a velocity profile employing a histogram is used to factor in the elevation angle dependence in the ego-motion estimation providing an velocity estimator inclusive of the elevation angles of the targets. As a means to track the ego-motion and elevation angle across the frames, 2-D EKF was employed. The histogram provides an initial ego-motion estimate which serves as an input for the EKF. Over the multiple

number of frames, the histogram proves to provide an improved initial ego-motion estimate.

The target tracking using the 2-D EKF provides a means by which the ego-motion can be tracked across frames and helps in conjunction with the velocity histogram to produce an improved ego-motion estimate, which in turn improves the elevation angle estimates of the respective targets. The EKF does tracks the states of the target and since stationary targets are dealt with in the application, the perceived velocity of the target, in practice is the velocity of the car. These improved ego-motion estimates are used to estimate the elevation angle information using the geometry. Subsequently, the elevation angle estimates can be used to compute the Z-coordinates which then generates a 3-Dimensional map giving a visualization on the height information of the targets. The height information helps in classifying those targets as something that an automobile can pass through, over or under. For one random realisation of 30 targets, the proposed algorithm created a 3-Dimensional map with a margin of error using the Z-coordinates providing the height information required for the classification procedure. However, the improvement in ego-velocity over the number of frames can help in lowering the Z-coordinate estimation error, thereby, improving the height classification procedure.

Through Monte Carlo simulations on a testbench created in MATLAB software that replicates the hardware and the application scenario, the viability of the proposed algorithm using a velocity histogram is confirmed. Comparisons were drawn between the approaches with and without histogram to understand the improvement and the effect or improvement it has on the bias. An improvement in the range of 0.06km/h - 0.08km/h was seen in the ego-velocity estimates using the histogram approach. The effect of SNR on the proposed algorithm is such that a deviation of around 0.2km/h - 0.4km/h is found for SNR of 10 dB as opposed to 0.07km/h - 0.14km/h for SNR of 30 dB. The improvement in bias was also validated at the frame level and is found to be consistent in performance of ego-motion estimation when compared to the algorithm without the histogram approach. The experimental validation using NXP radar was subsequently done to validate and to estimate the ego-motion and the 3-Dimensional map of the surroundings simultaneously. Using the four real-measurement data sets acquired, the ego-motion was estimated, using which elevation angles of the detected targets were calculated. Using the subsequent Z coordinate estimation, the height of the targets were estimated with a margin of error.. The estimation of ego-velocity was found to be accurate as the ground speed of the vehicle was recorded to be 15km/h. Using the elevation angles, the 3-Dimensional objects such as the lamp post and the side board was reconstructed and was able to create a realistic 3-Dimensional map providing the height information.

6.1.1. Challenges met during this thesis project

- **Experimental Validation during COVID**

  The final phase of testing the simulation data with the real-measurement was faced with a huge challenge due to the COVID situation and inability to conduct the required test cases for experimental validation. The real measurement data had to be collected from another project and was only able to use a certain section of the data to validate [46].

- **Using direct path detections**

  Due to time constraint and also to validate the detections and its respective associations to the target, the direct path detections were only considered. However, the incorporation of the indirect path detections can be done in the future work to improve the height classification.

6.2. Future Recommendations

In this section, based on the observations and the limitations of the proposed algorithm, the recommendations/-suggestions which can provide an improvement in the height classification of the targets are given below:

6.2.1. 3-Dimensional EKF

From the results shown in the Chapter 4.1, we can observe that the estimates of the elevation angle and the ego-velocity does not converge to their respective true value. This is due to the constraint brought in by the application of the 2-Dimensional Extended Kalman Filter, as we are not tracking the elevation angle explicitly. This can be improved by applying a 3-Dimensional Kalman Filter by defining the states involving the elevation angle and tracking it across frames. The application of 3-D EKF in radar tracking has been documented [47].

6.2.2. Indirect path method

During the internship at NXP, a binary classification algorithm was developed using the combination of direct path and indirect path in determining the traversability of the road objects [39]. However, the elevation angle and the azimuth angle was not incorporated into the project. On the contrary, utilizing the idea of combining the indirect path detections and the direct path detections can help in the association and also in the elevation angle tracking which can be a future prospect in this research topic. When there are multiple detections, there can be an association made between the direct path and the indirect path in terms of the range and velocity. However, it does not necessarily mean it belongs to the same target without the information of the DoA and DoD. In the later stage, an initial attempt was successfully done in being able to distinct the multipaths in terms of DoA and DoD using a simple phase comparison monopulse technique. This angle information can be used to associate the multipaths to the target which can help in the clustering phase of the algorithm in the future.

6.2.3. Experimental test cases

The results of the proposed algorithm can be validated and quantified in further by having multiple experimental test cases which can be a future aspect in carrying forward the research. Multiple targets of varying height, for instance, a bridge and different target structures can be placed in front of the car for the validation of the proposed algorithm and can help in optimizing and increasing the robustness of the algorithm. Moving targets in different distributions can also help in understanding the behaviour of the histogram and its responses to extreme cases, making the proposed algorithm universal.

References

[1] C. Waldschmidt, J. Hasch, and W. Menzel, "Automotive Radar — From First Efforts to Future Systems," *IEEE Journal of Microwaves*, vol. 1, no. 1, pp. 135–148, 2021. doi: 10.1109/JMW.2020.3033616.

[2] Z. Slavik, O. Bringmann, W. Rosenstiel, and Y. Eldar, "Implications and methods for co-existing automotive radar and communication systems," Oct. 2018. doi: 10.1109/ACSSC.2018.8645513.

[3] S. Shirvani Moghaddam and S. Monfared, "A Comprehensive Performance Study of Narrowband DOA Estimation Algorithms," *International Journal on Communications Antenna and Propagation*, vol. 1, pp. 396–405, Aug. 2011.

[4] M. Schoor and B. Yang, "High-resolution angle estimation for an automotive FMCW radar sensor," Jan. 2007.

[5] R. Feng, F. Uysal, and A. Yarovoy, "Target localization using MIMO-monopulse: Application on 79 ghz fmcw automotive radar," in *2018 15th European Radar Conference (EuRAD)*, 2018, pp. 59–62. doi: 10.23919/EuRAD.2018.8546566.

[6] A. Laribi, M. Hahn, J. Dickmann, and C. Waldschmidt, "Vertical Doppler beam sharpening goes self parking," in *2018 IEEE Radar Conference (RadarConf18)*, 2018, pp. 0383–0388. doi: 10.1109/RADAR.2018.8378589.

[7] D. Kellner, M. Barjenbruch, K. Dietmayer, J. Klappstein, and J. Dickmann, "Instantaneous lateral velocity estimation of a vehicle using Doppler radar," in *Proceedings of the 16th International Conference on Information Fusion*, 2013, pp. 877–884.

[8] D. Kellner, M. Barjenbruch, J. Klappstein, J. Dickmann, and K. Dietmayer, "Instantaneous ego-motion estimation using Doppler radar," in *16th International IEEE Conference on Intelligent Transportation Systems (ITSC 2013)*, 2013, pp. 869–874. doi: 10.1109/ITSC.2013.6728341.

[9] ——, "Instantaneous ego-motion estimation using multiple Doppler radars," in *2014 IEEE International Conference on Robotics and Automation (ICRA)*, 2014, pp. 1592–1597. doi: 10.1109/ICRA.2014.6907064.

[10] T. Miyasaka, Y. Ohama, and Y. Ninomiya, "Ego-motion estimation and moving object tracking using multilayer LIDAR," in *2009 IEEE Intelligent Vehicles Symposium*, 2009, pp. 151–156. doi: 10.1109/IVS.2009.5164269.

[11] Y. Fuke and E. Krotkov, "Dead reckoning for a lunar rover on uneven terrain," in *Proceedings of IEEE International Conference on Robotics and Automation*, vol. 1, 1996, 411–416 vol.1. doi: 10.1109/ROBOT.1996.503811.

[12] M. Wada, K. S. Yoon, and H. Hashimoto, "High accuracy road vehicle state estimation using extended kalman filter," in *ITSC2000. 2000 IEEE Intelligent Transportation Systems. Proceedings (Cat. No.00TH8493)*, 2000, pp. 282–287. doi: 10.1109/ITSC.2000.881069.

[13] R. van Gaalen. "Localization of Autonomous Vehicle using 1D Automotive Radar Sensor." (2020), [Online]. Available: http://resolver.tudelft.nl/uuid:e6a7f14e-97ea-4b67-a6d4-b90eaa040f75 (visited on 01/09/2020).

[14] NXP Semiconductors. "TEF810X Fully-Integrated 77 GHz Radar Transceiver." (2019), [Online]. Available: https://www.nxp.com/products/radio-frequency/radar-transceivers/tef810x-fully-integrated-77-ghz-radar-transceiver:TEF810X.

[15] V. Winkler, "Range Doppler detection for automotive FMCW radars," in *2007 European Microwave Conference*, 2007, pp. 1445–1448. doi: 10.1109/EUMC.2007.4405477.

[16] S. Orru. " FMCW radar based communication for automotive applications." (2020), [Online]. Available: http://resolver.tudelft.nl/uuid:c88d778f-3ff6-4efc-9ec4-57e04858d9f1 (visited on 07/16/2020).

[17] G.-H. Park, Y.-K. Seo, and H.-N. Kim, "Range-Doppler Domain-Based DOA Estimation Method for FM-Band Passive Bistatic Radar," *IEEE Access*, vol. 8, pp. 56 880–56 891, 2020. doi: 10.1109/ACCESS.2020.2981957.

[18] J. Li and P. Stoica, "MIMO Radar with Colocated Antennas," *IEEE Signal Processing Magazine*, vol. 24, no. 5, pp. 106–114, 2007. doi: 10.1109/MSP.2007.904812.

[19] A. M. Haimovich, R. S. Blum, and L. J. Cimini, "MIMO Radar with Widely Separated Antennas," *IEEE Signal Processing Magazine*, vol. 25, no. 1, pp. 116–129, 2008. doi: 10.1109/MSP.2008.4408448.

[20] J. J. M. de Wit, W. L. van Rossum, and A. J. de Jong, "Orthogonal waveforms for FMCW MIMO radar," in *2011 IEEE RadarCon (RADAR)*, 2011, pp. 686–691. doi: 10.1109/RADAR.2011.5960625.

[21] J. D. P. S. Sinha, *Millimeter-Wave Antennas: Configurations and Applications*. Springer, 2016.

[22] F. Uysal, *Lecture notes in Introduction to Automotive Radar Signal Processing*. ET4169-Microwaves, Radar and Remote Sensing, TU-Delft, April, 2019.

[23] P. Gupta and S. Kar, "MUSIC and improved MUSIC algorithm to estimate direction of arrival," in *2015 International Conference on Communications and Signal Processing (ICCSP)*, 2015, pp. 0757–0761. doi: 10.1109/ICCSP.2015.7322593.

[24] S. Kharel, "Performance Comparison Between MUSIC And ESPRIT Algorithms For Direction Estimation Of Arrival Signals," 2013. [Online]. Available: https://commons.und.edu/theses/1557.

[25] G. O. Manokhin, Z. T. Erdyneev, A. A. Geltser, and E. A. Monastyrev, "MUSIC-based algorithm for range-azimuth FMCW radar data processing without estimating number of targets," in *2015 IEEE 15th Mediterranean Microwave Symposium (MMS)*, 2015, pp. 1–4. doi: 10.1109/MMS.2015.7375471.

[26] R. Roy and T. Kailath, "ESPRIT-estimation of signal parameters via rotational invariance techniques," *IEEE Transactions on Acoustics, Speech, and Signal Processing*, vol. 37, no. 7, pp. 984–995, 1989. doi: 10.1109/29.32276.

[27] P. Häcker and B. Yang, "Single snapshot DOA estimation," *Advances in Radio Science*, vol. 8, pp. 251–256, Oct. 2010. doi: 10.5194/ars-8-251-2010.

[28] J. R. Guerci, *Space Time Adaptive Processing for Radar*. Artech House, 2003.

[29] W. Bürger. "Space-Time Adaptive Processing: Fundamentals." (2006), [Online]. Available: https://www.sto.nato.int/publications/STO%20Educational%20Notes/RTO-EN-SET-086/EN-SET-086-06.pdf.

[30] A. Howard, "Real-time stereo visual odometry for autonomous ground vehicles," in *2008 IEEE/RSJ International Conference on Intelligent Robots and Systems*, 2008, pp. 3946–3952. doi: 10.1109/IROS.2008.4651147.

[31] H. Badino, "A Robust Approach for Ego-Motion Estimation Using a Mobile Stereo Platform," Jan. 2004, pp. 198–208, isbn: 978-3-540-69864-7. doi: 10.1007/978-3-540-69866-1_15.

[32] B. Kitt, A. Geiger, and H. Lategahn, "Visual odometry based on stereo image sequences with RANSAC-based outlier rejection scheme," in *2010 IEEE Intelligent Vehicles Symposium*, 2010, pp. 486–492. doi: 10.1109/IVS.2010.5548123.

[33] S. Clark and G. Dissanayake, "Simultaneous localisation and map building using millimetre wave radar to extract natural features," in *Proceedings 1999 IEEE International Conference on Robotics and Automation (Cat. No.99CH36288C)*, vol. 2, 1999, 1316–1321 vol.2. doi: 10.1109/ROBOT.1999.772543.

[34] M. Dissanayake, P. Newman, S. Clark, H. Durrant-Whyte, and M. Csorba, "A solution to the simultaneous localization and map building (SLAM) problem," *IEEE Transactions on Robotics and Automation*, vol. 17, no. 3, pp. 229–241, 2001. doi: 10.1109/70.938381.

[35] K. Yokoo, S. Beauregard, and M. Schneider, "Indoor Relative Localization with Mobile Short-Range Radar," in *VTC Spring 2009 - IEEE 69th Vehicular Technology Conference*, 2009, pp. 1–5. doi: 10.1109/VETECS.2009.5073602.

[36] A. Macaveiu and A. Câmpeanu, "Automotive radar target tracking by Kalman filtering," in *2013 11th International Conference on Telecommunications in Modern Satellite, Cable and Broadcasting Services (TELSIKS)*, vol. 02, 2013, pp. 553–556. doi: 10.1109/TELSKS.2013.6704439.

[37] M. A. Richards, *Fundamentals of Radar Signal Processing*. US: McGraw-Hill Professional, 2005, isbn: 0071444742. [Online]. Available: https://mhebooklibrary.com/doi/book/10.1036/0071444742.

[38] A. Laribi, M. Hahn, J. Dickmann, and C. Waldschmidt, "Vertical digital beamforming versus multipath height finding," in *2017 IEEE MTT-S International Conference on Microwaves for Intelligent Mobility (ICMIM)*, 2017, pp. 99–102. doi: 10.1109/ICMIM.2017.7918866.

[39] A. Vijayaraghavan, A. Koppelaar, and F. Laghezza, "Short Range Height Classification in FMCW Radar," in *2020 17th European Radar Conference (EuRAD)*, 2021, pp. 116–119. doi: 10.1109/EuRAD48048.2021.00040.

[40] A. Laribi, M. Hahn, J. Dickmann, and C. Waldschmidt, "A new height-estimation method using FMCW radar Doppler beam sharpening," in *2017 25th European Signal Processing Conference (EUSIPCO)*, 2017, pp. 1932–1396. doi: 10.23919/EUSIPCO.2017.8081546.

[41] D. Oh and J. Lee, "Low Complexity Range-Azimuth FMCW Radar Sensor Using Joint Angle and Delay Estimation without SVD and EVD," *IEEE Sensors Journal*, vol. 15, pp. 1–1, Sep. 2015. doi: 10.1109/JSEN.2015.2428814.

[42] S. Gogineni and A. Nehorai, "Monopulse MIMO Radar for Target Tracking," *IEEE Transactions on Aerospace and Electronic Systems*, vol. 47, no. 1, pp. 755–768, 2011. doi: 10.1109/TAES.2011.5705707.

[43] W. Kederer and J. Detlefsen, "Direction of arrival (DOA) determination based on monopulse concepts," in *2000 Asia-Pacific Microwave Conference. Proceedings (Cat. No.00TH8522)*, 2000, pp. 120–123. doi: 10.1109/APMC.2000.925736.

[44] R. Feng, F. Uysal, P. Aubry, and A. Yarovoy, "MIMO-Monopulse Target Localization for Automotive Radar," *IET Radar, Sonar Navigation*, vol. 12, Aug. 2018. doi: 10.1049/iet-rsn.2018.5013.

[45] J. Zhang, H. Liu, J. Li, and C. Han, "Research on the mono-pulse phase comparison angle measurement algorithm of MIMO radar," in *The 2012 International Workshop on Microwave and Millimeter Wave Circuits and System Technology*, 2012, pp. 1–4. doi: 10.1109/MMWCST.2012.6238151.

[46] N. Petrov, O. Krasnov, and A. G. Yarovoy, "Auto-Calibration of Automotive Radars in Operational Mode Using Simultaneous Localisation and Mapping," *IEEE Transactions on Vehicular Technology*, vol. 70, no. 3, pp. 2062–2075, 2021. doi: 10.1109/TVT.2021.3058778.

[47] P. Aditya, E. Apriliani, D. Arif, and K. Baihaqi, "Estimation of three-dimensional radar tracking using modified extended kalman filter," *Journal of Physics: Conference Series*, vol. 974, p. 012 071, Mar. 2018. doi: 10.1088/1742-6596/974/1/012071.

A

Validation Code Example

The validation of the approach was first tested for simulation excluding the elevation angle parameter of the targets using the algorithm below, the result of which proved to be a success in tracking the azimuth angle of the target as well as the ego-motion estimate.

Algorithm 2 Extended Kalman Filter in ego-Velocity estimation (Excl. Elevation Angle)

Input: R_d, θ, v_{ego} **Output**: v_{ego}, θ

procedure EKF(v_{ego})
  if $p = 1$ **then** ▷ p - Frame number
    Initialize $\theta_{p,k} = \theta_{RD}$ ▷ θ from the r-D processing
    Extract the v_{ego} estimate from the histogram: $v_{ego,p} = histfunc(v_{r,k}, \cos(\theta_k))$
  else
    Extract the v_{ego} estimate from the histogram: $v_{ego,p} = histfunc(v_{r,k}, \cos(\theta_{KF,p,k})$
  end
  Estimate states of the system, $\boldsymbol{E}(S_p)$ ▷ Equation 3.21
  Obtain radar measurement data of the targets, $\boldsymbol{E}(Z_p)$ ▷ Equation 3.22
  Compute Jacobian matrix, $\boldsymbol{H}_j$ ▷ Mapping radar measurements
  Compute Kalman gain, $\boldsymbol{K}_p$ ▷ Equation 3.36
  Update system states, $\boldsymbol{E}(S_p)$ ▷ Equation 3.37
  Predict system states,$\boldsymbol{E}(S_{p+1})$ ▷ Equation 3.38
  Estimate azimuth angles: $\theta_{\text{KF,p+1,k}}$ ▷ Utilized in Step 6
  Compute average of the ego-velocity estimates over K targets ▷ Final ego-velocity estimate

B

Coordinate Conversion function Derivations

The derivations involved in the computation of the matrix elements in $\boldsymbol{M}(S_p)$ are given below:

$$\begin{bmatrix} \frac{df}{dx} & \frac{df}{d\dot{x}} & \frac{df}{dy} & \frac{df}{d\dot{y}} \\ \frac{dg}{dx} & \frac{dg}{d\dot{x}} & \frac{dg}{dy} & \frac{dg}{d\dot{y}} \\ \frac{dh}{dx} & \frac{dh}{d\dot{x}} & \frac{dh}{dy} & \frac{dh}{d\dot{y}} \end{bmatrix} \tag{B.1}$$

The matrix elements can be calculated as follows:

$$\frac{df}{dx} = \frac{d\left(R_d\right)}{dx} = \frac{d\left(\sqrt{x^2+y^2}\right)}{dx} = \frac{1}{2\sqrt{x^2+y^2}} \cdot 2x = \frac{x}{\sqrt{x^2+y^2}} \tag{B.2}$$

$$\frac{dg}{dx} = \frac{d(\theta)}{dx} = \frac{d(\text{atan}(y/x))}{dx} = \frac{1}{1+(y/x)^2} \cdot y \cdot \frac{-1}{x^2} = \frac{-y}{x^2+y^2} \tag{B.3}$$

$$\begin{aligned} \frac{dh}{dx} &= \frac{d\left(v_r\right)}{dx} = \frac{d\left(v \cdot \cos(\theta-\beta)\right)}{dx} = \frac{d\left(v \cdot \cos(\text{atan}(y/x)-\beta)\right.}{dx} \\ &= \sqrt{\dot{x}^2+\dot{y}^2} \cdot -\sin(\text{atan}(y/x)-\beta) \cdot \frac{d\theta}{dx} \\ &= v \cdot -\sin(\theta-\beta) \cdot \frac{dg}{dx} \end{aligned} \tag{B.4}$$

Similarly with respect to y,

$$\frac{df}{dy} = \frac{d\left(R_d\right)}{dy} = \frac{d\left(\sqrt{x^2+y^2}\right)}{dy} = \frac{1}{2\sqrt{x^2+y^2}} \cdot 2y = \frac{y}{\sqrt{x^2+y^2}} \tag{B.5}$$

$$\frac{dg}{dy} = \frac{d(\theta)}{dx} = \frac{d(\text{atan}(y/x))}{dx} = \frac{1}{1+(y/x)^2} \cdot \frac{1}{x} = \frac{x}{x^2+y^2} \tag{B.6}$$

$$\begin{aligned} \frac{dh}{dy} &= \frac{d\left(v_r\right)}{dy} = \frac{d\left(v \cdot \cos(\theta-\beta)\right)}{dy} = \frac{d\left(v \cdot \cos(\text{atan}(y/x)-\beta)\right.}{dy} \\ &= v \cdot -\sin(\theta-\beta) \cdot \frac{dg}{dy} \end{aligned} \tag{B.7}$$

$$\begin{aligned} \frac{dh}{d\dot{x}} &= \frac{d\left(v_{\mathrm{r}}\right)}{d\dot{x}} = \frac{d(v \cdot \cos(\theta-\beta))}{d\dot{x}} = \frac{d\left(\sqrt{\dot{x}^2+\dot{y}^2} \cdot \cos(\theta-\beta)\right)}{d\dot{x}} \\ &= \frac{\dot{x} \cdot \cos(\theta-\beta) - \dot{y}\sin(\theta-\beta)}{\sqrt{\dot{x}^2+\dot{y}^2}} \\ &= \frac{\dot{x}\cos(\theta-\beta) - \dot{y}\sin(\theta-\beta)}{v} \end{aligned} \tag{B.8}$$

Similarly,

$$\begin{aligned}\frac{dh}{d\dot{y}} &= \frac{d\left(v_{\mathrm{r}}\right)}{d\dot{y}} = \frac{d(v \cdot \cos(\theta-\beta))}{d\dot{y}} = \frac{d\left(\sqrt{\dot{x}^2+\dot{y}^2}\cdot\cos(\theta-\beta)\right)}{d\dot{y}} \\ &= \frac{\dot{y}\cdot\cos(\theta-\beta)+\dot{x}\sin(\theta-\beta)}{\sqrt{\dot{x}^2+\dot{y}^2}} \\ &= \frac{\dot{y}\cos(\theta-\beta)+\dot{x}\sin(\theta-\beta)}{v}\end{aligned} \tag{B.9}$$